Dynamics of Atmospheres and Oceans, 14 (1989) 125–174
Elsevier Science Publishers B.V., Amsterdam – Printed in The Netherlands

REGIONAL PRIMITIVE EQUATION MODELING AND ANALYSIS OF THE POLYMODE DATA SET

MICHAEL A. SPALL*
Center for Earth and Planetary Physics, Harvard University, Cambridge, MA (U.S.A.)

(Received September 6, 1988; revised February 22, 1989; accepted March 6, 1989)

ABSTRACT

Spall, M.A., 1989. Regional primitive equation modeling and analysis of the POLYMODE data set. Dyn. Atmos. Oceans, 14: 125–174.

A regional, hybrid coordinate, primitive equation (PE) model is applied to a 60-day period of the POLYMODE data set. The initialization techniques and open boundary conditions introduced by Spall and Robinson are shown to produce stable, realistic, and reasonably accurate hindcasts for the 2-month data set. Comparisons with quasi-geostrophic (QG) modeling studies indicate that the PE model reproduced the jet formation that dominates the region more accurately than did the QG model. When the PE model used boundary conditions that were partially adjusted by the QG model, the resulting fields were very similar to the QG fields, indicating a rapid degradation of small-scale features near the boundaries in the QG calculation. A local term-by-term primitive equation energy and vorticity analysis package is also introduced. The full vorticity, horizontal divergence, kinetic energy, and available gravitational energy equations are solved diagnostically from the output of the regional PE model. Through the analysis of a time series of horizontal maps, the dominant processes in the flow are illustrated. The individual terms are also integrated over the region of jet formation to highlight the net balances as a function of time. The formation of the deep thermocline jet is shown to be due to horizontal advection through the boundary, baroclinic conversion in the deep thermocline and vertical pressure work, which exports the deep energy to the upper thermocline levels. It is concluded here that the PE model reproduces the observed jet formation better than the QG model because of the increased horizontal advection and stronger vertical pressure work. Although the PE model is shown to be superior to the QG model in this application, it is believed that both PE and QG models can play an important role in the regional study of mid-ocean mesoscale eddies.

1. INTRODUCTION

Regional ocean modeling has been an important and rapidly advancing topic of oceanographic research in the past 10 years (Haidvogel, 1983). The

* Current address: National Center for Atmospheric Research Boulder, CO 80303, U.S.A.

0377-0265/89/$03.50

first limited-area models contained barotropic, quasi-geostrophic physics with periodic boundary conditions (Bretherton and Karweit, 1975; Haidvogel et al., 1980). Although these models were useful for the analysis of simplified, spatially homogeneous flows, the need for more realistic physics and true open ocean boundary conditions was readily apparent. The addition of baroclinicity allowed for the study of problems more representative of the real ocean by including the effects of stratification (Miller at al., 1981). The extension to 'open ocean' boundary conditions has not been as straightforward. Open boundary conditions should allow for the free passage of phenomena from within the domain through the boundary, and, in addition, information from the surrounding ocean to be fed into the region through the boundaries. Mathematically, this problem has not yet been solved for either the quasi-geostrophic or primitive equations (Bennett and Kloeden, 1978; Oliger and Sundstrom, 1978). In practical terms, boundary conditions for the quasi-geostrophic equations first proposed by Charney et al. (1950) have been used to obtain stable, realistic and useful model calculations for a variety of quasi-geostrophic studies (Robinson and Walstad, 1987). There has been considerable work on open boundary conditions for the primitive equations (PE) for special cases and simplified flows (Orlanski, 1976; Raymond and Kuo, 1984), but as yet no general boundary conditions exist for PE models.

Applications of open ocean models include the study of: spatially homogeneous flows; eddy–eddy and eddy–mean-flow interactions; local topographic forcing; eddy generation; and free ocean jets. The models are generally initialized with analytic representations of idealized flow situations or fields derived from *in situ* and remotely sensed data. The evolution of idealized flows is useful to isolate specific geophysical fluid dynamic phenomena and study its dependence on variations of the physical parameters. The use of dynamical models to evolve observed flow systems is useful for dynamical interpolation and interpretation of individual synoptic representations of the flow field. The dynamical interpolation in time is useful to visualize how the flow field evolved from an initial state to a final observed state. Spatial interpolation allows for higher order analysis of the fields than can be obtained directly from the data. Quasi-geostrophic models have been used to hindcast and forecast open ocean mesoscale data sets since the early 1980s (Robinson et al., 1986; Robinson and Walstad, 1987). To the author's knowledge, a primitive equation model has never been used to hindcast or forecast an open ocean mesoscale data set.

Regional ocean models have typically contained quasi-geostrophic physics for several reasons. The quasi-geostrophic approximation is valid for flows which have small Rossby number ($R = V/fl$), long time-scales compared to a day, small length-scales compared to the planetary scale, and a vertical

scale much less than the horizontal scale. Primitive equation physics, in addition to including terms that may be important to the mesoscale phenomena, allow for a variety of high-frequency waves that are generally not directly contained in the mesoscale fields of interest. These waves may be spuriously generated through initial adjustment processes or inaccurate boundary conditions. The presence of these waves may mask the mesoscale processes or even interact with and contaminate the larger scale signal (Daley, 1981). In addition, the quasi-geostrophic equations are generally less expensive to solve than are the primitive equations. For flows that satisfy the quasi-geostrophic approximation, regional QG models have been very useful for the study of local mesoscale phenomena.

POLYMODE was a joint U.S.–U.S.S.R. experiment designed to: describe and map the mesoscale variability for several eddy cycles; yield estimates of the local dynamical balances; and obtain a statistical description of the eddy field in the western North Atlantic (Robinson, 1982). The Synoptic Dynamical Experiment (SDE) was a subset of the larger program located on the southern edge of the Gulf Stream recirculation gyre. Characteristic of this region are strong, deep thermocline jets (McWilliams, 1983a) and small mesoscale eddies (Shen et al., 1986). The time- and space-scales of the mesoscale variability are 50–150 days and 50–150 km (The MODE Group, 1978). Energy and vorticity budgets of this data set have indicated the importance of eddies in the mean heat, vorticity, and momentum balances (Bryden, 1982; Owens et al., 1982; McWilliams, 1983b). This data set has also been used to develop and demonstrate the methodology of initializing an open ocean quasi-geostrophic model for hindcast and forecast studies of real ocean data (Walstad, 1987).

The dynamically adjusted fields generated by numerical models are very useful for energy and vorticity budgets. Use of the numerical models to dynamically interpolate the fields allows for accurate higher order derivatives, which may not be attainable directly from observations. Basin-averaged quantities calculated for PE (Bryan and Cox, 1967; Holland and Lin, 1975; Robinson et al., 1977) and quasi-geostrophic (Holland, 1978) models have been useful in the study of eddy generation, eddy dissipation and eddy–mean-flow interaction in the North Atlantic. Horizontal maps of individual terms in the quasi-geostrophic vorticity and consistent energy equations have been used to illustrate the dominant physical processes responsible for a variety of dynamic events in regional calculations. Pinardi and Robinson (1986, 1987) demonstrate the methodology of using a quasi-geostrophic model to dynamically interpolate observed fields and then apply an energy and vorticity analysis (EVA) scheme to interpret the evolution of those fields in the POLYMODE and OPTOMA regions. Robinson et al. (1988) use the same approach to study the dynamics and energetics of ring formation events in the Gulf Stream region.

The methodology of using regional dynamical models and analysis techniques has been developed and demonstrated with quasi-geostrophic physics. For applications in which the quasi-geostrophic approximation is not valid, regional PE modeling and a consistent term-by-term energy and vorticity analysis must be used. A new open ocean, hybrid coordinate PE model was introduced by Spall and Robinson (1989) (hereafter SR) for regional applications. In this paper, the application of that model to the hindcasting of real ocean data in a limited region is demonstrated. In addition, a new term-by-term energy, vorticity and divergence analysis package with primitive equation physics is introduced. The derivation of the analysis equations from the discrete solution of the primitive equations gives rise to apparent sources of vorticity and horizontal divergence. This is because the form of the advection operators in the momentum equations conserves energy but not enstrophy. Monitoring of these terms indicates the error introduced by the advective operator and under what circumstances an enstrophy conserving scheme may be desirable. Analysis of the dynamically interpolated fields is used to determine the dominant processes of the flow and the range of validity of quasi-geostrophy in the region.

In section 2, the numerical model and dynamical equations are presented. The primitive equation energy and vorticity analysis (PRE-EVA) equations are given in section 3. Important aspects of the solution procedure compatible with the dynamical model and a physical interpretation of the PRE-EVA terms are included in the Appendix. The POLYMODE data set is reviewed in section 4. The PE model calculations are presented and discussed along with the observations and a quasi-geostrophic calculation by Walstad (1987) (hereafter W87) in section 5. The PRE-EVA analysis results are discussed in section 6. Finally, conclusions from this study are given in section 7.

2. THE NUMERICAL MODEL

The numerical model used in this study is an open ocean, hybrid coordinate, PE model, based on the standard model of Bryan and Cox (1967). The primitive equations assume that the fluid is hydrostatic and that the Boussinesq approximation is valid. For hydrostatic motion, all acceleration terms are neglected in the vertical momentum equation except gravity; this is valid for 'thin' fluids, i.e. the vertical length-scale is much less than the horizontal length-scale (Phillips, 1966). The Boussinesq approximation replaces the density by its mean value everywhere except when it is multiplied by the gravitational acceleration (Phillips, 1969). Observations indicate that this is a good approximation because the density of seawater varies by only about 5%, even less when compressibility effects are not included. Only a brief review of the governing equations and solution procedure will be given here.

For a more detailed description of the model and its applications to ocean problems, the reader is referred to SR.

Hybrid coordinates involve a simple transformation of variables in the vertical for all model levels below a prescribed depth, z_c

$$\sigma(x, y, z) = \frac{z - z_c}{H'} \tag{1}$$

where

$$H' = H(x, y) - z_c \qquad z_c \le z \le H(x, y) \tag{2}$$

In this way the model surfaces follow the bottom topography ($H(x, y)$) smoothly over the entire domain below z_c; all levels shallower than z_c remain horizontal. The vertical resolution below z_c is increased in shallow regions, such as over seamounts or along a coast. Because the surfaces on which the prognostic variables are calculated are no longer horizontal, cross terms appear in the equations of motion. Differences can be minimized by the definition of the sigma coordinate vertical velocity as

$$\omega = \frac{1}{H'}\left[w - \sigma\left(uH'_x + vH'_y\right)\right] \tag{3}$$

Application of the conservation of momentum gives the x, y and z momentum equations, written below in hybrid coordinates

$$u_t + \frac{1}{H'}(H'uu)_x + \frac{1}{H'}(H'vu)_y + (u\omega)_\sigma - fv$$
$$= -\frac{1}{\rho_0}(P_x - g\sigma H'_x\rho) + F_{mh} + F_{mz} \tag{4}$$

$$v_t + \frac{1}{H'}(H'uv)_x + \frac{1}{H'}(H'vv)_y + (v\omega)_\sigma + fu$$
$$= -\frac{1}{\rho_0}(P_y - g\sigma H'_y\rho) + F_{mh} + F_{mz} \tag{5}$$

$$P = H'_g\int_0^\sigma \rho \, d\sigma \tag{6}$$

where u, v, and w are the velocities in the zonal, meridional and sigma coordinate directions, respectively (f is the coriolis parameter), F_{mh} and F_{mz} are parameterizations of the horizontal and vertical viscous forces, P is the pressure, ρ is the density and g is the gravitational acceleration. A Shapiro filter has been used for the horizontal subgrid-scale parameterization in each of the experiments in this paper. This filter is a highly scale-selective

smoothing operation originally developed for meteorological applications (Shapiro, 1970); its use in ocean modeling is documented by Robinson and Walstad (1987) and Spall and Robinson (1989). For sloping surfaces, depths below z_c, the filter operation has been projected on to the horizontal as described by SR.

Conservation of mass for an incompressible fluid is used to derive the continuity equation

$$\frac{1}{H'}(H'u)_x + \frac{1}{H'}(H'v)_y + \omega_\sigma = 0 \tag{7}$$

The energy equation without sources or sinks may be written in terms of the temperature (T) and salinity (S) as

$$T_t + \frac{1}{H'}(H'uT)_x + \frac{1}{H'}(H'vT)_y + (\omega T)_\sigma = F_{hh} + F_{hz} \tag{8}$$

$$S_t + \frac{1}{H'}(H'uS)_x + \frac{1}{H'}(H'vS)_y + (\omega S)_\sigma = F_{hh} + F_{hz} \tag{9}$$

An equation of state is used to close the system

$$\rho = \rho(T, S, P) \tag{10}$$

For levels above the transformation depth, these equations are valid with $H' = z_c$ and the standard primitive equations are retained.

The hybrid coordinate formulation gives a uniform vertical resolution of the upper ocean (depths less than z_c). This may be important to obtain a realistic finite difference representation of a continuous density profile for model initialization that maintains the desired pressure gradients in the horizontal (i.e. geostrophic balance). Using the standard sigma coordinates, in regions of sloping bottom topography the vertical resolution of the base of the thermocline or upper Eckman layer will be dependent on horizontal position. For marginally resolved vertical profiles, this variation can give results that are artificially dependent on horizontal position.

If the model is initialized at rest, and there is no dissipation, the fields remain at rest. However, as is common with sigma coordinate type models, the addition of horizontal dissipation will modify the motionless density surfaces slightly. Over time, this will introduce pressure forces that cause a small acceleration of the flow. The extent to which the density surfaces are modified has been reduced in this model by projecting the dissipation on to horizontal surfaces and by allowing the model levels to remain horizontal in the upper thermocline, the region of the largest vertical gradients in density.

The numerical model solves eqns. (4)–(10) subject to initial and boundary conditions. The vertical boundary conditions are a rigid lid at the surface

and no normal flow through the bottom

$$w = 0 \qquad z = 0 \tag{11}$$

$$w = uH_x + vH_y \qquad z = H(x, y) \tag{12}$$

The horizontal open boundary conditions are analogous to the Charney et al. (1950) boundary conditions first proposed for the quasi-geostrophic equations. The density and normal velocity are specified on all horizontal boundary points and the tangential velocity is specified on inflow points only. On outflow, two-dimensional vorticity equations are solved for the vertical vorticity and the barotropic vertical vorticity. The finite difference form of vorticity is then inverted to obtain the tangential velocity. The vorticity equations and the calibration of the boundary conditions are given in SR.

3. THE PRE-EVA ANALYSIS PACKAGE

PRE-EVA is a primitive equation energy and vorticity analysis package to be used with the output of the PE model described in section 2. It solves the vorticity and divergence form of the horizontal momentum equations and the kinetic and available gravitational energy equations.

The methodology of using the PRE-EVA analysis package is straightforward. The dynamical model is first used to simulate an open ocean flow either as a dynamical interpolator of observed systems (hindcast or forecast) or for basic geophysical process experiments. The analysis package is then applied diagnostically to the output from the numerical model. Each of the terms in the analysis equations are calculated to produce a time series of horizontal maps. Through the interpretation of these maps, the dominant processes of the flow field can be illustrated. The terms may also be integrated over subregions of the flow that are critical to the evolution in order to highlight the dominant balances. The analysis routine may only be applied to outputs from the dynamical model presented in section 2. Observed systems, analytical fields, or data sets generated by another numerical model are not in consistent balance with the discrete form of the dynamical equations. Attempts to analyze these fields directly will yield results that may not have reasonable physical interpretations.

3.1. PRE-EVA equations

The horizontal momentum and heat equations may be used to derive equations that are useful in analysis of the PE model results. In this section,

the vertical vorticity, horizontal divergence, kinetic energy and available gravitational energy equations will be derived from the primitive equations.

The velocity field is first decomposed into the rotational (geostrophic) and irrotational components via the streamfunction ψ and velocity potential χ

$$\mathbf{v} = k \times \nabla\psi + \nabla\chi \tag{13}$$

This leads to the variables relative vorticity, ζ, and horizontal divergence, D

$$\zeta = \nabla^2\psi \qquad D = \nabla^2\chi \tag{14}$$

The vertical vorticity equation is derived from the horizontal momentum equations by cross differentiating the momentum equations and summing to eliminate the pressure term. Substituting for the streamfunction and velocity potential, the final vorticity equation is written below (Batteen, 1984), valid for depths above z_c. The equation is also written in symbolic form for future discussion

$$\begin{aligned}[\zeta_t]^{qg} = &-[J(\psi, \zeta)]^{qg} - [J(\psi, f)]^{qg} - [f\nabla^2\chi]^{qg} - [\nabla\chi\cdot\nabla f]^{lb} \\ &-[\nabla\chi\cdot\nabla\zeta]^{fb} - [\zeta\nabla^2\chi]^{fb} - [w\zeta_z]^{fb} - [\nabla w\cdot\nabla\psi_z]^{fb} - J(w, \chi_z) \\ &+[B\zeta_{zz}]^{qg} + [F_h]^{qg}\end{aligned} \tag{15}$$

$$\dot{R} = -\Delta_0 F_R - \Delta_0 F_P - fD - \Delta_1 F_P - \Delta_1 F_R - RD - \delta f_R - \delta\xi_0 - \delta\xi_1 + F_z + F \tag{16}$$

Each term in the original equation has been given a superscript according to the order to which it is retained in the consistent expansion from quasi-geostrophic to primitive equation physics (Lorenz, 1960). The superscript qg indicates that only those terms are retained in the quasi-geostrophic approximation, lb are the additional terms retained for the linear balance equations, the fb terms are also included for the full balance equations, and all of the terms are included for the full primitive equations. A scaling analysis is used to derive these and other sets of equations intermediate in physics between primitive equation and quasi-geostrophy by Gent and McWilliams (1983).

To derive the horizontal divergence equation, the momentum equations are operated on with the vector operator $\nabla\cdot()$ and added. The final form is given below, with the appropriate superscripts as defined for the vorticity equation

$$\begin{aligned}D_t = &-[\nabla^2(P/\rho_0)]^{qg} + [f\nabla^2\psi]^{qg} + [\nabla f\cdot\nabla\psi]^{lb} - J(f, \chi) \\ &-[\nabla\cdot((k\times\nabla\psi)\cdot\nabla(k\times\nabla\psi))]^{fb} - \nabla\cdot(k\times\nabla\psi)\cdot\nabla^2\chi) - \nabla \\ &\cdot(\nabla\chi\cdot\nabla(k\times\nabla\psi)) - \nabla\cdot(\nabla\chi\cdot\nabla^2\chi) - \nabla w\cdot(k\times\nabla\psi)_z - \nabla w\cdot\nabla\chi_z \\ &+[BD_{zz}]^{qg} + [F_h]^{qg}\end{aligned} \tag{17}$$

$$\dot{D} = -D_2 P + fR - \Delta_0 D_P - \Delta_1 D_P - \Delta_0\Delta_0 - \Delta_0\Delta_1 - \Delta_1\Delta_0 - \Delta_1\Delta_1 - \delta\Delta_0 - \delta\Delta_1 + F_z + F \tag{18}$$

The kinetic energy equation is derived by multiplying the x, y and z momentum equations by u, v and w, respectively, and then summing. The final kinetic energy equation is written below, where $K = \frac{1}{2}(u^2 + v^2)^{1/2}$. Because $w \ll u$, v, it is dropped from the definition of K.

$$\frac{\partial K}{\partial t} = -\nabla \cdot (\mathbf{u}K) - \nabla \cdot \left(\frac{p}{\rho_0}\mathbf{u}\right) + g\Delta w - AK_{zz} + F \tag{19}$$

$$\dot{K} = -\Delta F_K - \delta f_K - \Delta F_\pi - \delta f_\pi + b - F_z + F_h \tag{20}$$

The horizontal advection term and the divergence of pressure work have been broken up into the horizontal and vertical components in eqn. (20).

To obtain the available gravitational energy equation, the prognostic equation for density (analogous to eqn. (8) but for ρ) is multiplied by $-(\rho_0 g\Delta)/(\partial\tilde{\rho}/\partial z)$, where Δ is the perturbation density. The available gravitational energy is defined as $A = g\Delta^2/(2\partial\tilde{\rho}/\partial z)$. When derived in this fashion, the buoyancy conversion term (b) between kinetic energy and available gravitational energy is equal and opposite in both equations. The use of prognostic temperature and salinity equations to solve the available gravitational energy equation is discussed in the Appendix. The horizontal advections have been split into their geostrophic ($\mathbf{u}_0$) and ageostrophic ($\mathbf{u}_1$) components

$$\frac{\partial A}{\partial t} = -\nabla \cdot (\mathbf{u}_0 A) - \nabla \cdot (\mathbf{u}_1 A) - \frac{A}{2s} w \frac{\partial s}{\partial z} - g\Delta w - A_h A_{zz} + F \tag{21}$$

where $s = \partial\tilde{\rho}/\partial z$.

$$\dot{A} = -\Delta_0 F_A - \Delta_1 F_A - \delta\bar{\rho} - b - F_z + F_h \tag{22}$$

The physical interpretation of each of the PRE-EVA terms and details of the numerical solution procedure are given in the Appendix.

4. THE POLYMODE MARK II DATA SET

The POLYMODE mark II data set is a subset of the larger POLYMODE (The MODE Group, 1978) experiment. The region of analysis is centered at 29°N, 70°W, near the southern edge of the Gulf Stream recirculation region. The data consist of temperature profiles from expendable bathythermographs (XBTs) to a depth of 700 m, and a time series of velocity measurements from moored current meters at 700 and 1400 m. Analysis of the data and calculation of the three-dimensional streamfunction field was carried out by W87. A review of the procedure is given here.

Dynamic height relative to 700 m was calculated from the XBT profiles using a T–S relationship characteristic of the region. Space–time objective analysis techniques were used to map the upper ocean XBT data, which was irregularly spaced in both space and time on to uniform grids. The horizontal grid resolution was 15.625 km covering 281.25×281.25 km^2 (19×19), and maps were produced at 1-day intervals. Multivariate objective analysis techniques were used to combine the XBT and current meter data at 700 m. The objective analysis was also used to determine the value of the streamfunction at 1400 m to within a constant, which may vary in time. The constant, which is proportional to the mean density between 700 and 1400 m, was determined by a least-square fit to the baroclinic mode calculated from data above 700 m.

An estimate of the deep ocean flow was obtained by projecting the data levels on to the barotropic and first baroclinic modes. Analysis of the POLYMODE data set has shown that 98% of the variability in geostrophic streamfunction may be reproduced with the barotropic and first baroclinic modes alone (The MODE Group, 1978). The estimate of the first barotropic mode comes from current meters. Information about the baroclinic mode may be obtained from both XBT and current meter data, an even weighting of each estimate was used.

In the following discussion, the objectively analyzed XBT and current meter data will be referred to as the data and the observations. It must be pointed out that this is not strictly correct since the process of converting the raw data into uniform maps of streamfunction involves several steps and assumptions. In addition to measurement error, T–S relationships, objective analysis techniques, and geostrophic dynamics are all included in the derivation of the streamfunction reference field. The objectively analyzed data will also be referred to as MKII.

The period modeled by MARK II began on Julian day 3410 and extended to Julian day 3470. The fields at 3410, 3430 and 3450 are shown in Fig. 1,

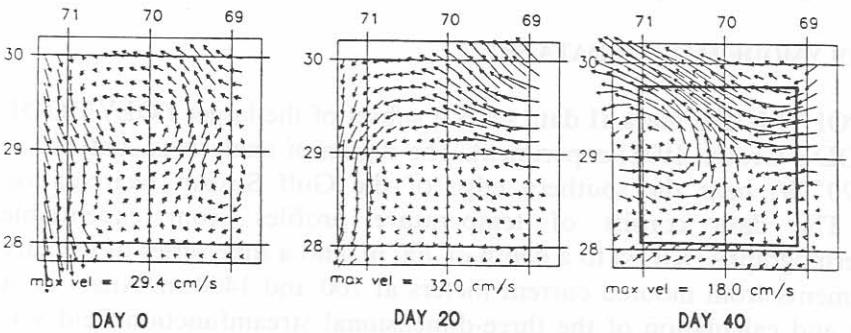

Fig. 1. Observed velocity at 400 m, days 3410, 3430 and 3450 (model days 0, 20 and 40).

days 0, 20 and 40, respectively. The initial condition is described by a southward flowing jet along the western boundary and a large cyclonic circulation filling the northern half of the domain. The maximum velocity at 400 m is almost 30 cm s^{-1}. On day 20 the southward jet has weakened and moved off to the west, and a strong westward jet has developed in the northeastern portion of the domain. The jet strengthens to a maximum velocity of ~ 35 cm s^{-1} and then drops off to ~ 18 cm s^{-1} near the end of the data set. The observed fields are highly variable and exhibit several events during this 60-day period.

5. MODEL SIMULATIONS

In this section, two PE model runs are carried out using the initial condition on Julian day 3410. Bottom topography has been included in each calculation and is shown in Fig. 2. The bottom gently slopes from 4900 m on the eastern boundary to just over 5200 m near the center of the southern boundary. Although it is relatively flat, the inclusion of bottom topography was found to significantly improve the results in both QG (Walstad, 1987) and PE (Spall, 1988) modeling studies. The level of the hybrid coordinate interface (z_c) is 2000 m. This value was chosen to give a uniform vertical resolution of the upper thermocline over variable topography and still place two levels in the deep without using a different set of vertical levels than was used for the observations or previous QG model calculations.

In the first calculation, PE-OA, the boundary information is derived directly from the objectively analyzed data set. For the second calculation, PE-DA, the boundary information is derived from the QG streamfunction field generated in the best simulation of the QG modeling studies done by W87. OA and DA indicate that the boundary conditions were objectively

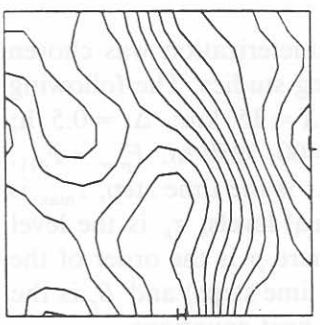

MIN=4900 MAX=5230 CI=27

Fig. 2. Bottom topography (m).

analyzed or dynamically adjusted, respectively. The boundary conditions are only partially adjusted, because in the transformation from the uniform grid used by the QG model to the B-grid used by the PE model, some of the interior information is used together with the boundary information. Because of the boundary conditions used in the QG model calculation, the mass flow through the boundary and the density on the boundary are the same as in the objectively analyzed data. The tangential velocity, or equivalently vorticity, is obtained at 1/2 grid point towards the interior of the domain and used information from the interior. Based on this comparison, the effect of using boundary information that has been dynamically adjusted by the quasi-geostrophic model can be assessed.

Extensive hindcast and forecast studies of the POLYMODE data set were carried out using the Harvard Open Ocean QG Model by W87. In this section, the best QG model simulation during the period 3410–3470 from those studies (QG-OA) will be analyzed in terms of the PE variables. Spall and Robinson (1989) compared PE and QG calculations of a simulated mesoscale eddy field designed after the POLYMODE data set and found the differences in the model calculations attributable to model physics and not model numerics. This gives confidence that any differences found in the model simulations are due to physics and not numerical methods or representation of model variables.

The PE model was initialized from the objectively analyzed streamfunction using the methods described by SR. The outermost grid point was stripped off of the data set to avoid the use of information derived from one-sided differences at the boundaries. Additional information that is required to initialize the temperature and salinity are the mean density and the T–S relationship characteristic of the region. The T–S curve is shown in Fig. 3a and the mean density as a function of depth is shown in Fig. 3b, each of these was obtained from the Levitus and Oort (1975) data set. Results from QG modeling studies of W87 are also discussed in terms of primitive equation variables.

The model discretization and subgrid-scale parameterization was chosen to be the same as was used in previous QG modeling studies. The following values were used in each of the experiments: $\Delta X = 15$ km; $\Delta t = 0.5$ h; $t_{\max} = 60$ days; $KZ = 6$; $z_k = 100, 400, 700, 1400, 2400, 3950$ m; $F_{pqr} = F_{411}$; $B_z = 5$ cm s^{-2}. ΔX is the horizontal grid spacing, Δt is the time step, $t_{\max}$ is the time of integration, KZ is the number of vertical levels, z_k is the level distribution, F_{pqr} is the Shapiro filter operation (where p is the order of the filter, q is the number of times it is applied every r time steps) and B_z is the vertical diffusion coefficient in the momentum and heat equations.

To evaluate the performance of the model calculations, basin-integrated quantities and PE variables will be compared with the objectively analyzed

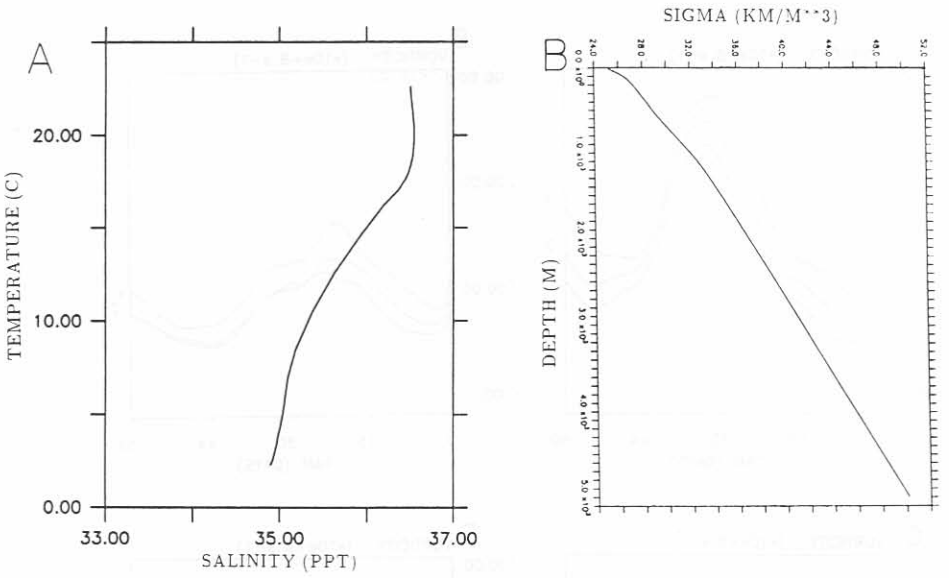

Fig. 3. (a) $T-S$ for POLYMODE region, (b) density versus depth.

data. Quantities that have been integrated over the entire region are useful to obtain a quick, qualitative assessment of the comparison between the two fields. The integrated quantities that will be compared are vorticity, kinetic energy and normalized root-mean-square (NRMS) differences of velocity (V_{NRMS}). The root-mean-square differences have been normalized by the RMS value of the observed velocity field. By directly comparing the field variables, the regions of agreement and disagreement can be determined and a characterization of the behavior made.

5.1. Averaged quantities

The basin-averaged vorticity as a function of time is shown in Fig. 4(a–d) for PE-OA, PE-DA, QG-OA and MKII. The number to the right of each curve refers to the model level. The growth of the westward flowing jet is clearly evident in MKII between days 15 and 30, Fig. 4d. During this time, the vorticity increases from 90 to 225 s^{-1} at 400 m. A similar response is seen at 100 and 700 m. As the jet weakens, the vorticity decreases sharply, but then increases slightly near the end. This peak in vorticity is reproduced much better in PE-OA than in PE-DA and QG-OA. The early growth rate of PE-OA compares well and the magnitude is just about right at 30 days of integration. The vorticity begins to decrease with the weakening jet, but levels off and then increases slightly at too large a value. In runs PE-DA and

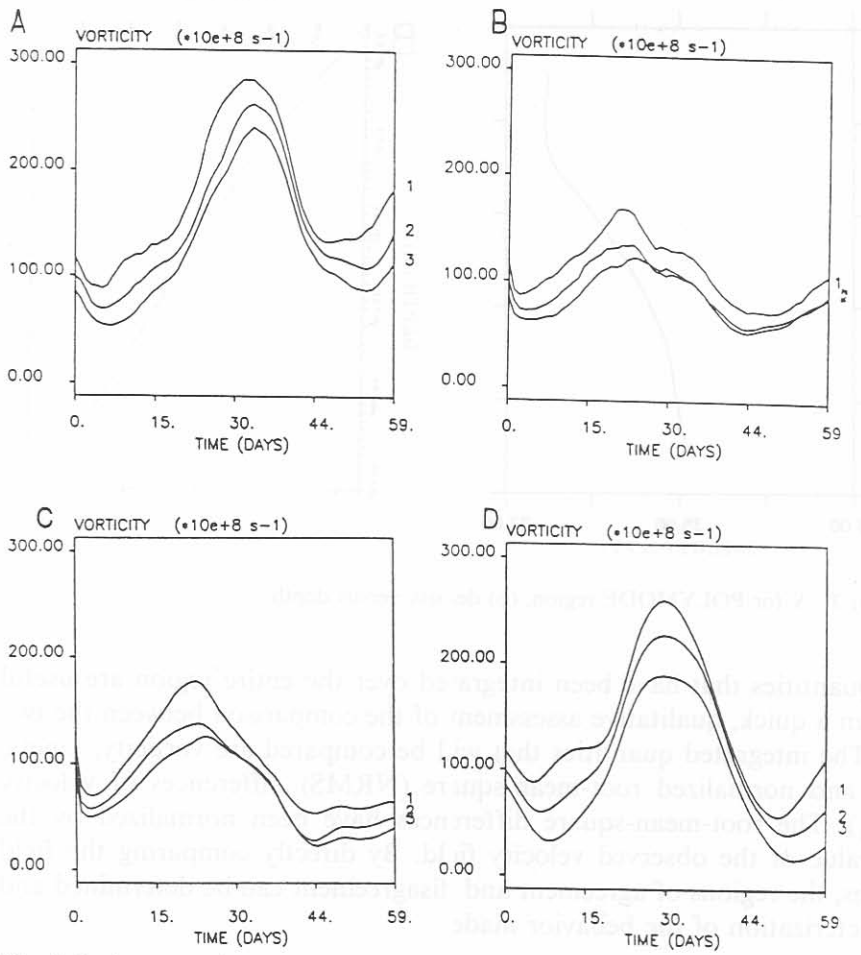

Fig. 4. Basin-averaged vorticity (a) PE-OA, (b) PE-DA, (c) QG-OA and (d) MKII.

QG-OA the vorticity is increasing at the correct rate early in the simulation, but peaks at 20 days and then begins to decrease. The strong peak at 30 days does not develop in either calculation.

In Fig. 5, the basin-averaged kinetic energy for the upper three levels is shown. The observations, Fig. 5d, show a large increase between days 15 and 30 as the jet develops in the northern part of the domain. The maximum at 30 days, is 160 cm^2 s^{-2} at 400 m. After 30 days the jet weakens and the kinetic energy rapidly decreases. The magnitude and time of formation of the peak is reproduced well in PE-OA (Fig. 5a) but the kinetic energy increases a little too fast as the jet is forming. The kinetic energy begins to drop off as the jet weakens, but then levels off on day 44 at too high a level. PE-DA (Fig. 5b) and QG-OA (Fig. 5c) produce a peak in energy, but they

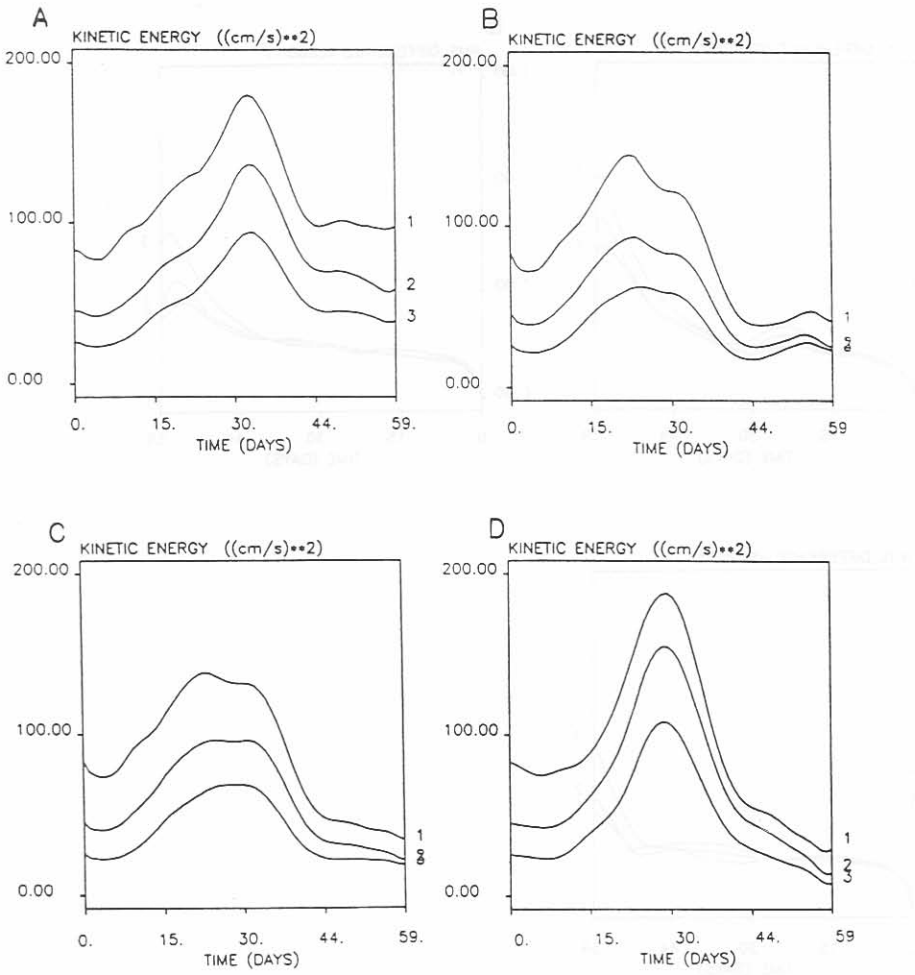

Fig. 5. Basin-averaged kinetic energy (a) PE-OA, (b) PE-DA, (c) QG-OA and (d) MKII.

occur too early and have magnitudes of only 90 and 95 $cm^2\ s^{-2}$, respectively, at 400 m. The growth rates are very similar to PE-OA for the first 20 days, but between days 20 and 30 the energy decreases slowly and then drops off very quickly toward the end.

The NRMS differences in the velocity fields relative to MKII are shown in Fig. 6. Each of the model calculations show an early adjustment period of 4 or 5 days, during which the NRMS difference grows to $\sim 30\%$. This remains almost constant out to day 15, and then there is a distinct local maximum in PE-OA that lasts 15 days, until day 30. During this time, the NRMS difference increases by $\sim 10\%$ at level two and 20% at level three. Level one only shows a slight increase. PE-DA and QG-OA do not show any

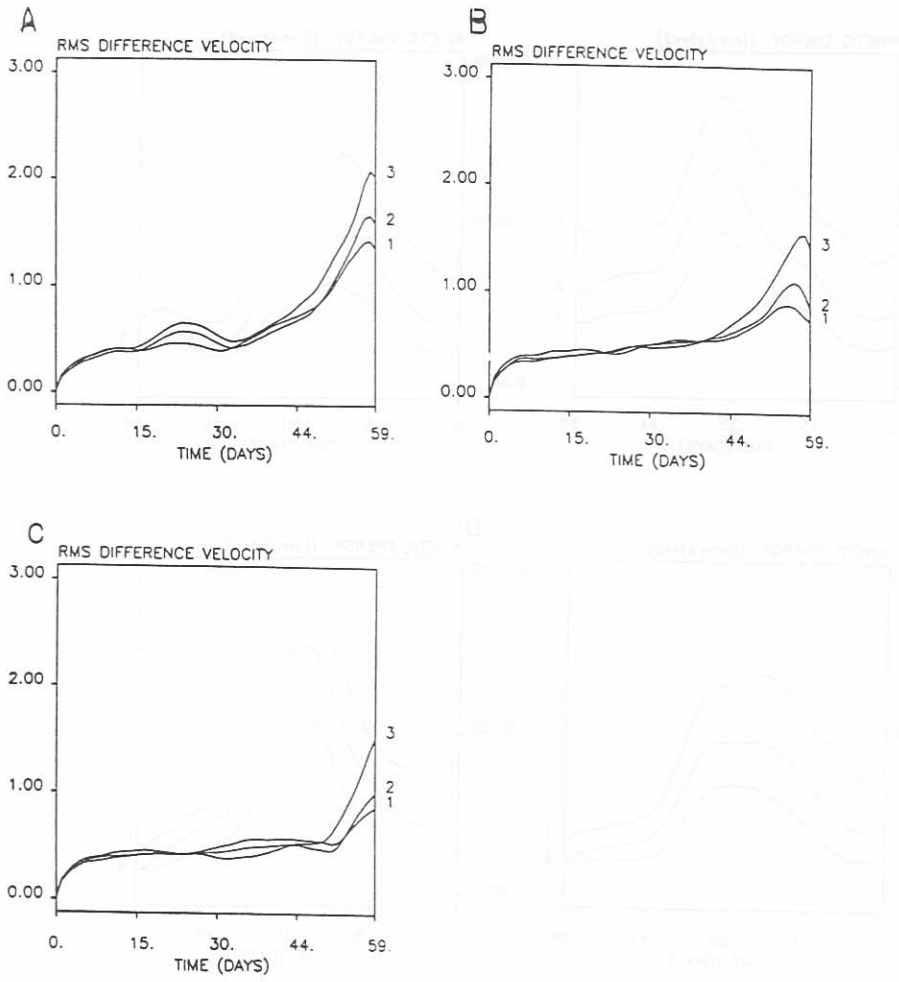

Fig. 6. Basin-averaged V_{NRMS} (a) PE-OA, (b) PE-DA, (c) QG-OA and (d) MKII.

significant increase during this period. For the next 15 days, days 30–45, the three calculations give very similar results, with QG-OA slightly lower. After day 45, the NRMS differences increase rapidly for all three runs. The V_{NRMS} in PE-DA and QG-OA are characterized by an initial adjustment period, uniform growth of $\sim 0.5\%$ day^{-1}, and then a rapid increase after day 45. PE-OA exhibits the same behavior, with the addition of a significant increase and decrease between days 15 and 30.

It is a little surprising that the NRMS velocity differences look so similar, while the vorticity and kinetic energy averages are quite different. This can be explained by considering what each of the quantities represents. Because vorticity is proportional to the derivative of the velocity it is a measure of

the extent of small-scale flow in the flow. The kinetic energy will be more strongly weighted by differences in the high velocity regions of the flow while V_{NRMS} is influenced equally by both the stronger and weaker flows. This suggests that PE-DA and QG-OA contain less small-scale flow and underestimate the strength of the northern jet between days 15 and 40. The local maximum observed in the V_{NRMS} of PE-OA occurs just as the jet is forming, its source will be discussed in section 6.3.

5.2. Velocity fields

A direct comparison between the velocity fields for PE-OA, PE-DA, QG-OA and MKII is shown in Fig. 7(a–c). The first row contains the velocity fields at 400 m and the second row is the difference between the model calculation and the observations. Proceeding from left to right, the fields are PE-OA, PE-DA, QG-OA and MKII. In general, the model results agree well with the observed fields. For the first 15 days of the calculation each of the fields looks about the same, Fig 7a. The southward jet is beginning to move out of the domain and the westward jet is just entering the northeast corner. Each of the model calculations have similar cyclonic and anticyclonic circulation in their difference fields. On day 30, Fig. 7b, the westward jet has strengthened and extended across the region and the southward jet is almost gone. The difference field for PE-OA shows an anticyclonic circulation contained in the western portion of the domain. Its magnitudes are large, about 15 cm s^{-1}, but it does not extend all the way into the jet-formation region. Runs PE-DA and QG-OA also have too much anticyclonic circulation, but which covers a much larger portion of the model domain. As a result, the southern edge of the forming jet is 10 cm s^{-1} weaker in those runs than in the data and PE-OA. The difference fields are almost identical for PE-DA and QG-OA. Near the end of the calculations, on day 50, the jet region compares very well between PE-OA and the data. Differences in the strength of the jet are less than 5 cm s^{-1}. Runs PE-DA and QG-OA produce a jet too broad in the eastern part of the domain and too weak in the western part. South of the jet, all of the model calculations produce a strong cyclonic circulation that is not observed in the data.

5.3. Density fields

The density fields at 400 m are shown in Fig. 8(a–c), for PE-OA, PE-DA, QG-OA and MKII. The initial baroclinic structure is characterized by a southward jet along the western boundary and a cyclonic eddy in the northern half of the domain. After 15 days, the jet is seen beginning to form in the northeast corner of the domain, Fig. 8a. Each of the model calcula-

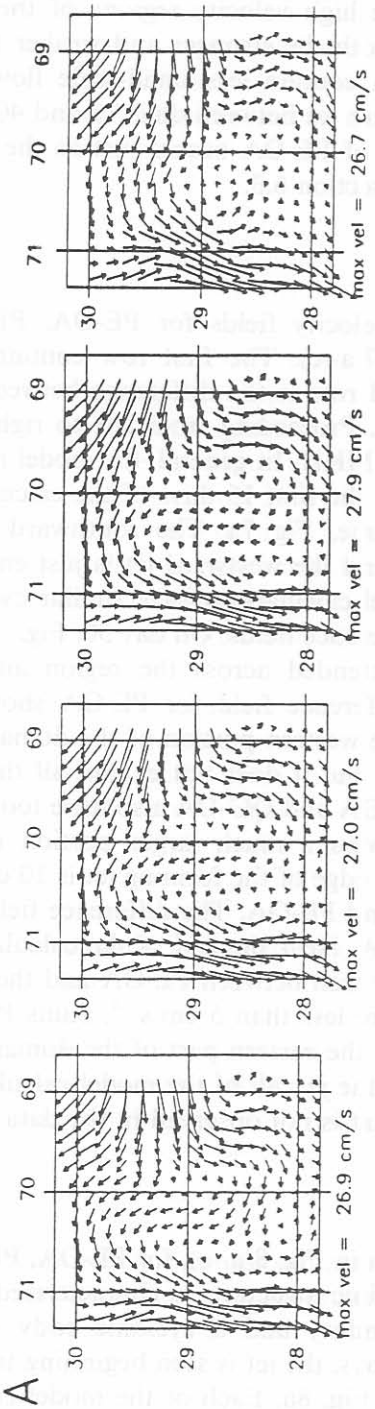

Fig. 7. Velocity (top row) and difference (bottom row) at 400 m. From left to right: PE-OA, PE-DA, QG-OA and MKII. (a) Day 15, (b) day 30 and (c) day 50.

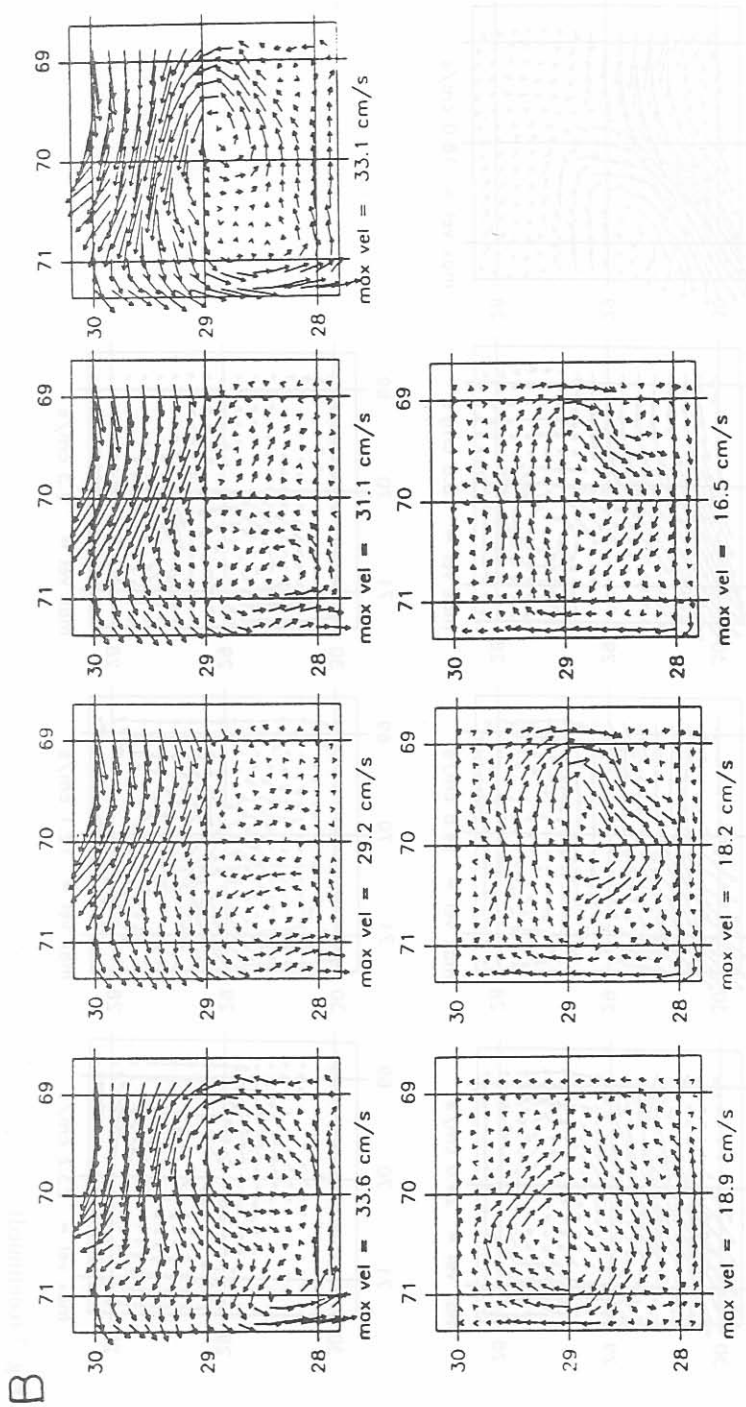

Fig. 7 (continued).

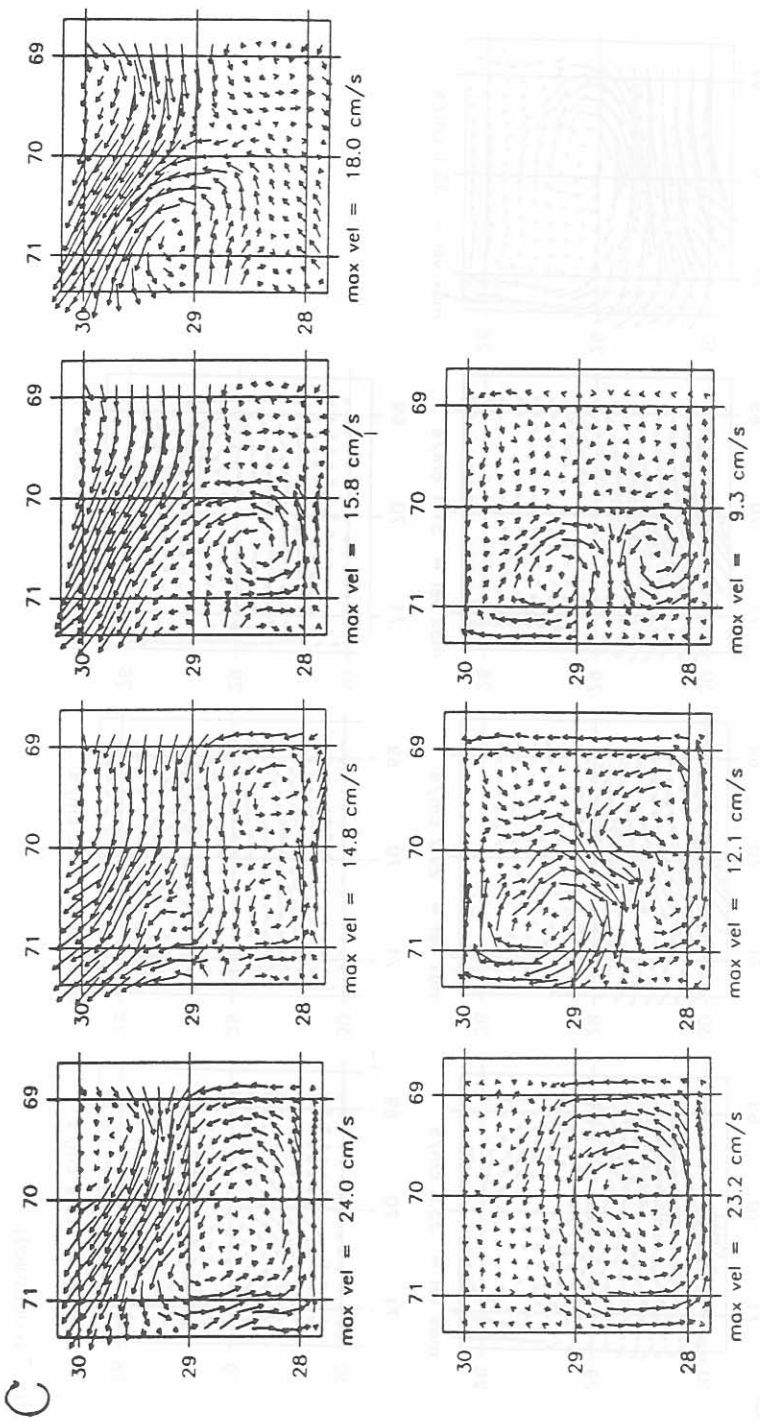

Fig. 7 (continued).

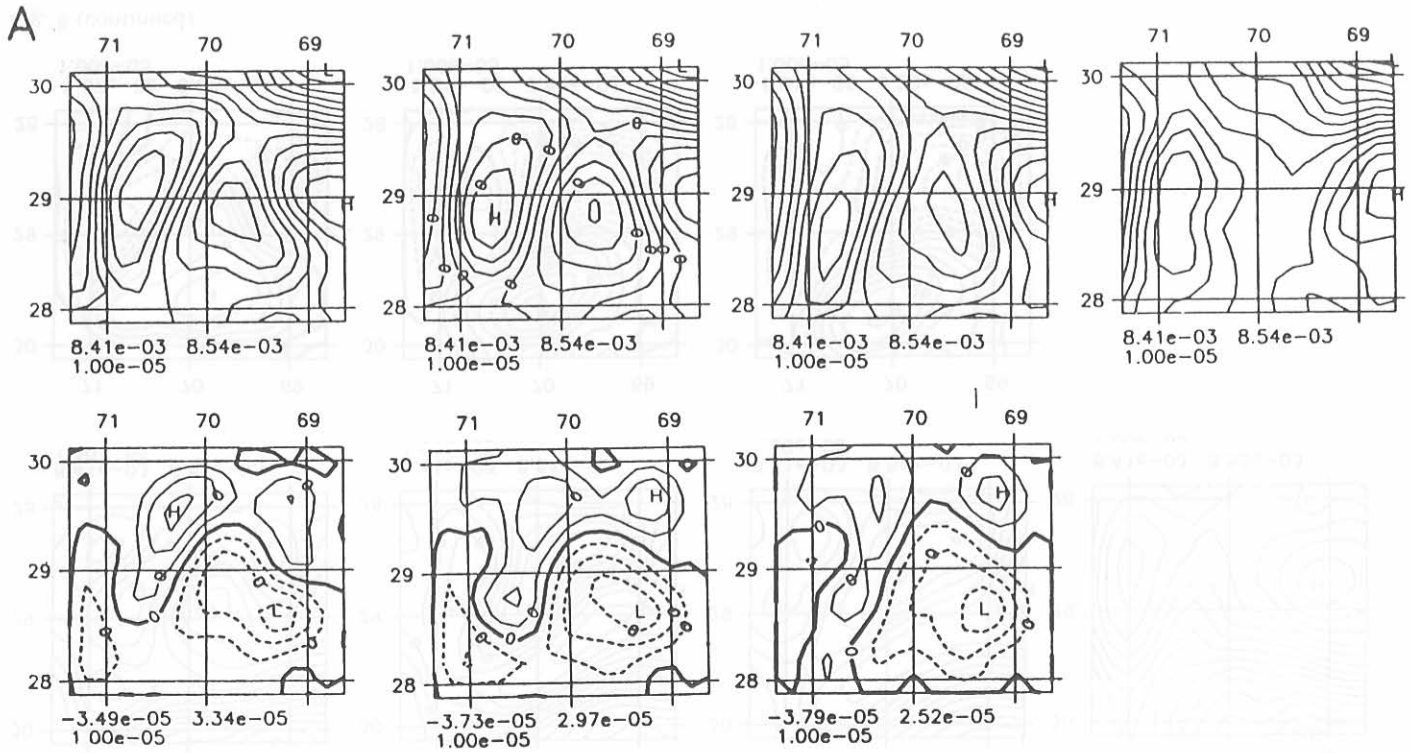

Fig. 8. Density (top row) and difference (bottom row) at 400 m. From left to right: PE-OA, PE-DA, QG-OA and MKII. (a) Day 15, (b) day 30 and (c) day 55.

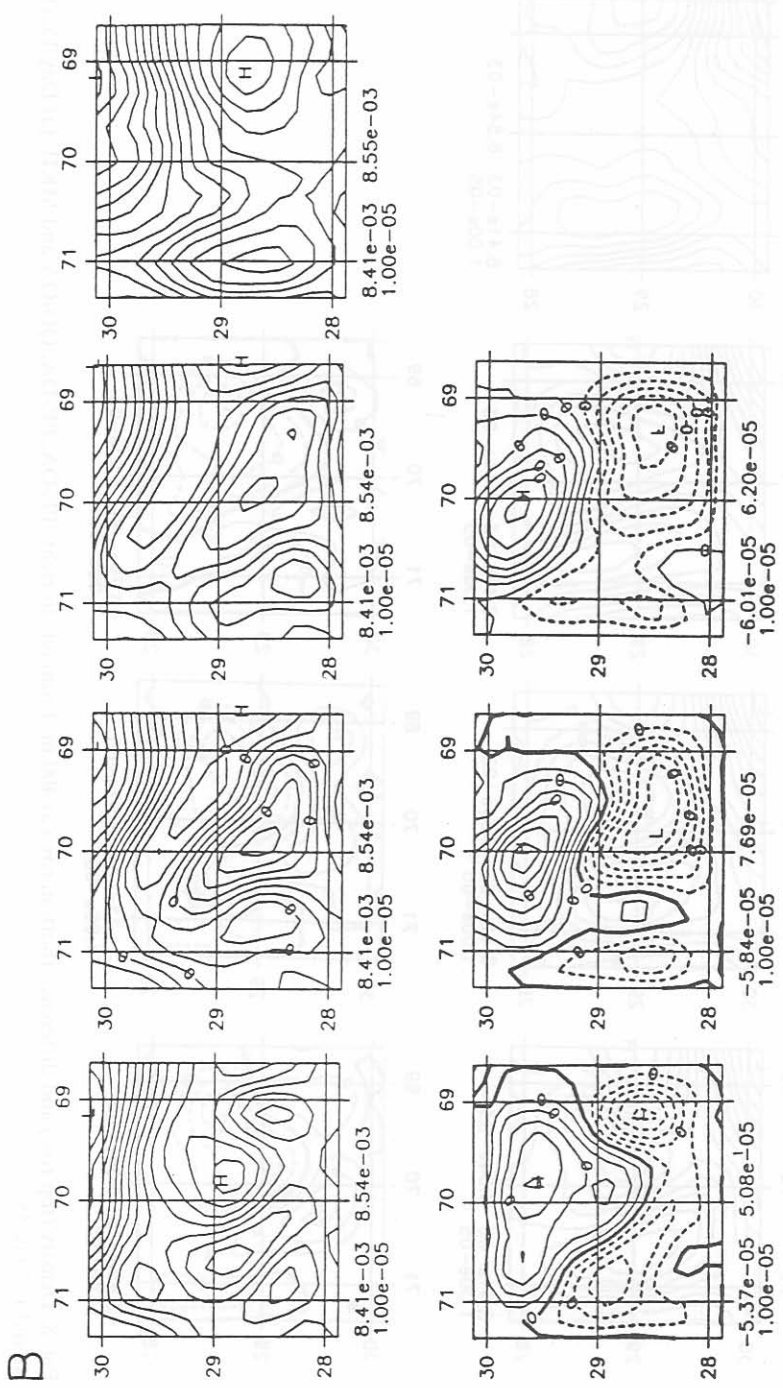

Fig. 8 (continued).

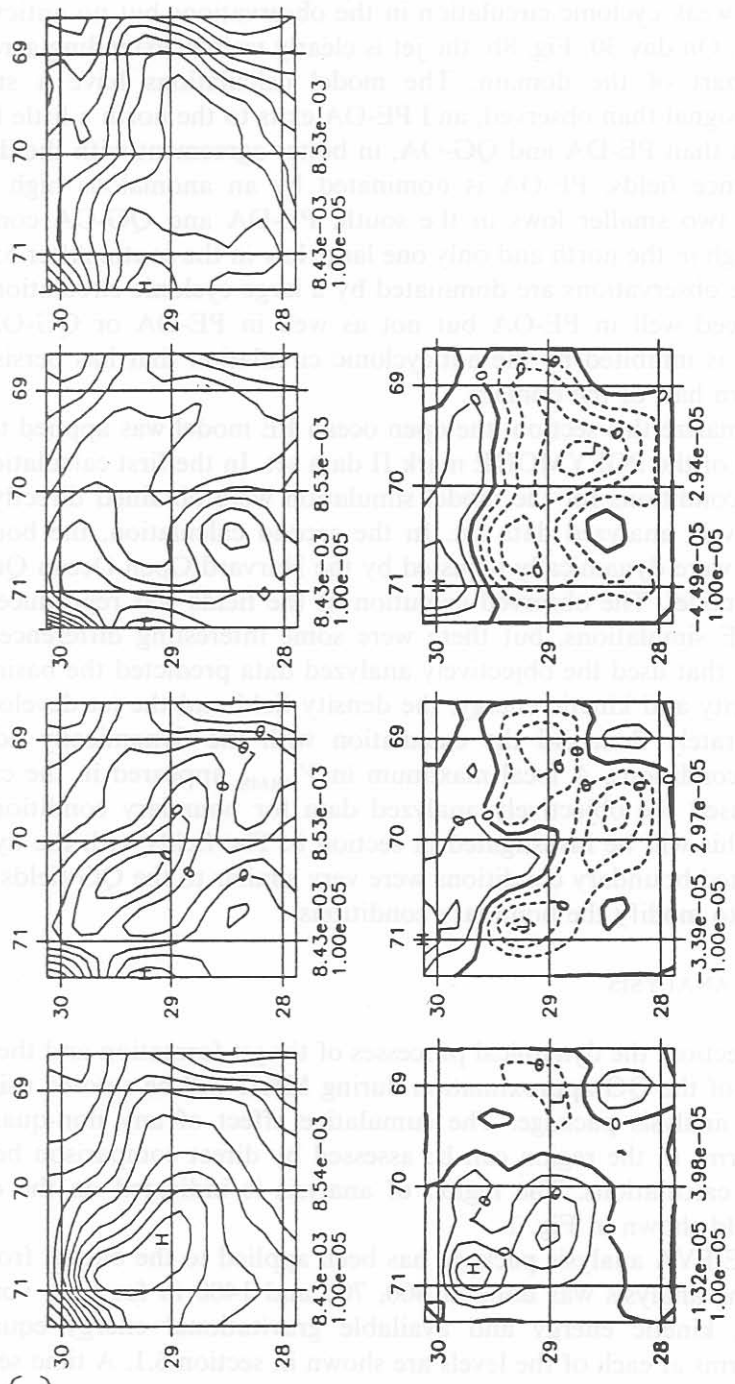

Fig. 8 (continued).

tions contain strong cyclonic (density high) and anticyclonic (density low) circulations in the western and eastern halves of the domain, respectively. There is a weak cyclonic circulation in the observations but no anticyclonic circulation. On day 30, Fig. 8b, the jet is clearly visible, extending across the northern part of the domain. The model calculations have a stronger baroclinic signal than observed, and PE-OA exits to the north a little further to the west than PE-DA and QG-OA, in better agreement with the data. In the difference fields, PE-OA is dominated by an anomalous high in the north and two smaller lows in the south. PE-DA and QG-OA contain a stronger high in the north and only one large low in the south. After 55 days, Fig. 8c, the observations are dominated by a large cyclonic circulation. This is reproduced well in PE-OA but not as well in PE-DA or QG-OA; the circulation is inhibited by the anticyclonic circulation that has persisted in the southern half of the domain.

To summarize this section, the open ocean PE model was applied to days 3410–3470 of the POLYMODE mark II data set. In the first calculation, the boundary conditions for the model simulation were obtained directly from the objectively analyzed data set. In the second calculation, the boundary conditions were dynamically adjusted by the Harvard Open Ocean Quasigeostrophic model. The observed evolution of the fields was reproduced well by both PE simulations, but there were some interesting differences. The calculation that used the objectively analyzed data predicted the basin-averaged vorticity and kinetic energy, the density field and the jet development more accurately than did the calculation with the dynamically adjusted boundary conditions. A local maximum in V_{NRMS} appeared in the calculation that used the objectively analyzed data for boundary conditions, the source of this will be investigated in section 6. The fields with the dynamically adjusted boundary conditions were very similar to the QG fields which were used to modify the boundary conditions.

6. PRE-EVA ANALYSIS

In this section, the dynamical processes of the jet formation and the range of validity of the QG approximation during MKII will be studied using the PRE-EVA analysis package. The cumulative effect of any non-quasi-geostrophic terms in the region can be assessed by direct comparison between the model calculations. The region of analysis is indicated on the day-40 velocity field shown in Fig. 1.

The PRE-EVA analysis package has been applied to the output from run PE-OA. The analysis was done at 400, 700 and 1400 m for each vorticity, divergence, kinetic energy and available gravitational energy equations. Selected terms at each of the levels are shown in section 6.1. A time series of

the balances integrated in a subregion containing the jet formation is discussed in section 6.2. The dominant balances and physical processes in the flow will be illustrated. In section 6.3, the analysis routine is used to understand what process is responsible for the better jet formation in PE-OA relative to PE-DA.

6.1. PRE-EVA balances

6.1.2. Vorticity equation

Horizontal maps of the dominant terms in the vertical vorticity equation at 1400 m are shown in Fig. 9(a–d). The streamfunction and relative vorticity are included on the left for reference. During the early part of the simulation (not shown here) the balance is mostly between $\dot{R}$ (time rate of change), ΔF_R (horizontal advection) and fD (horizontal divergence). On day 20, Fig. 9a, the jet is beginning to form in the eastern portion of the domain. The vorticity is contained in alternating large-scale patches across the north and east. Along the jet, $\dot{R}$ is nearly balanced by ΔF_R. These terms are characterized by alternating smaller scale patches traveling along the developing jet. This indicates that the eastern boundary is a source of relative vorticity to the region. The fD term, which is proportional to the horizontal divergence, is mostly very small scale near the northeast and southern boundaries. This is nearly balanced completely by the horizontal filter, F. Eight days later, Fig. 9b, the jet has strengthened and the meander is propagating to the west. Again, there is a clear separation of scales between the advection term and the horizontal divergence term. The filter acts only on the small-scale terms in fD, and it does not have a strong correlation with $\dot{R}$ or ΔF_R. On day 36, Fig. 9c, the jet has begun to move out of the region and a basin-scale circulation is developing. The wave pattern in $\dot{R}$ has almost left through the northwest and a new one is developing in the southeast corner. The advective balance is not as pure as earlier, as fD and F are active on slightly larger scales. Four days later, Fig. 9d, the jet has gone and a new flow is developing in the southeast. F and fD are balanced along the east and north in narrow alternating patches about 1 grid point wide parallel to the side boundaries. It is believed that these, and previous small-scale features near the boundaries, are gravity waves being generated at the horizontal boundaries and propagating toward the interior.

It is a little troubling that at times the filter is very large, however, it generally occurs near the boundaries and only on a small scale. The filter is removing what are believed to be gravity waves generated by small incompatibilities between the boundary conditions and the interior flow. The source of these waves is numerical, they are not believed to be representative of gravity waves present in the real POLYMODE mark II data set. This form

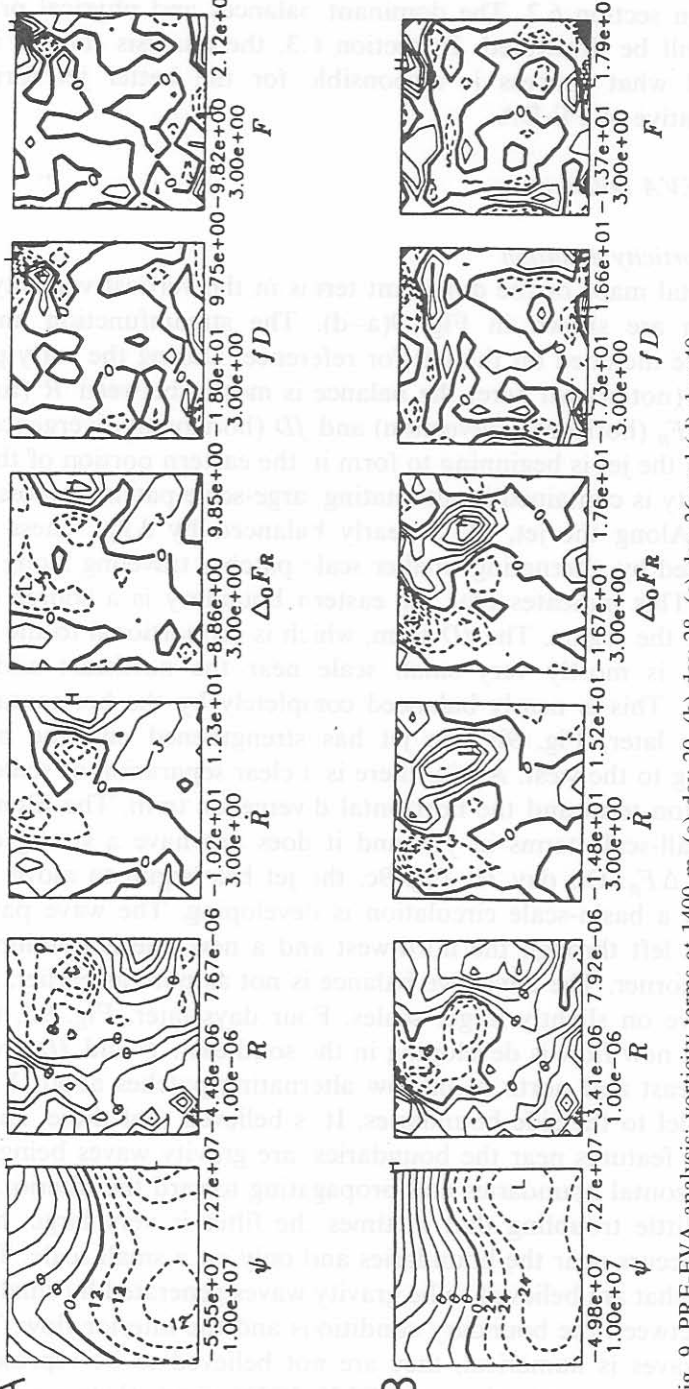

Fig. 9. PRE-EVA analysis: vorticity terms at 1400 m, (a) day 20, (b) day 28, (c) day 36 and (d) day 40.

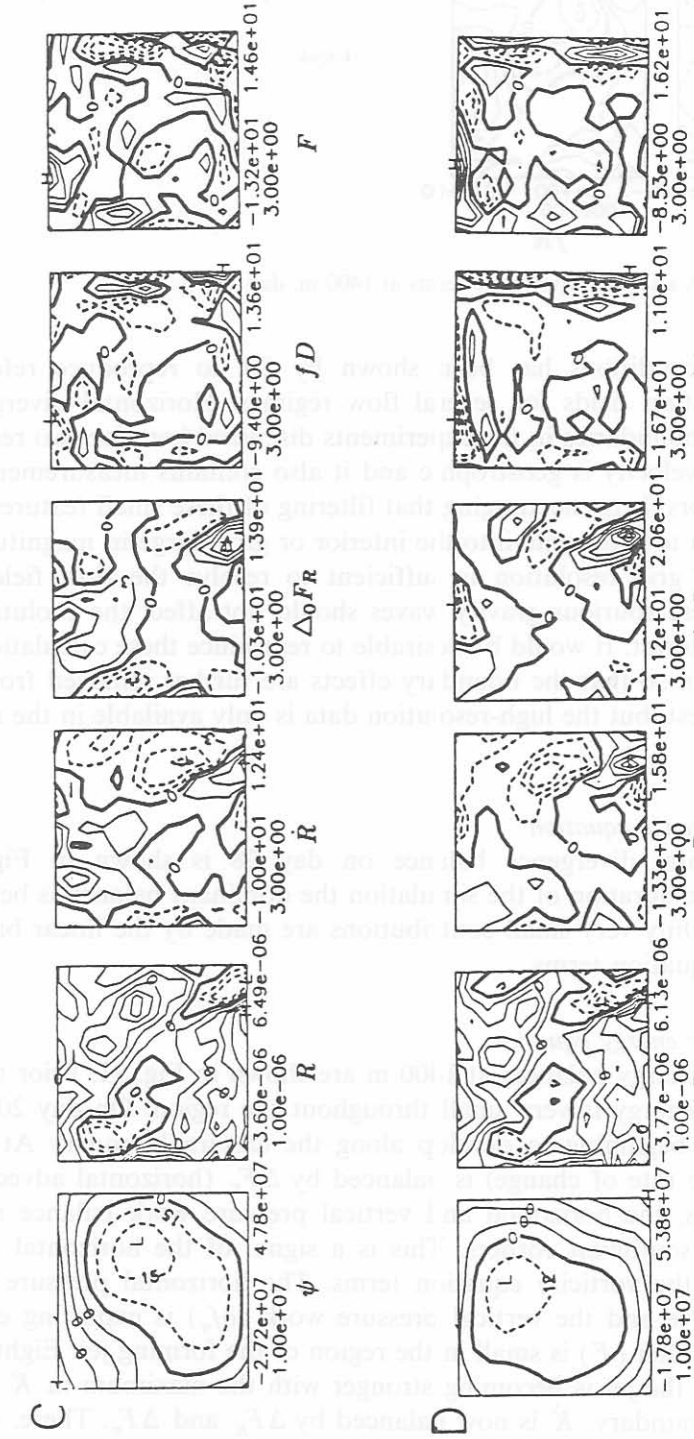

Fig. 9 (continued).

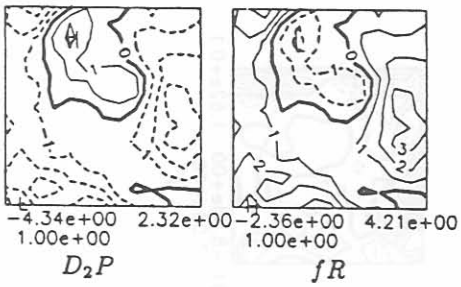

Fig. 10. PRE-EVA analysis: divergence terms at 1400 m, day 28.

of boundary conditions has been shown by SR to reproduce reference primitive equation fields for several flow regimes. Horizontal divergences arise near the boundaries in the experiments discussed here for two reasons. The observed velocity is geostrophic and it also contains measurement and processing errors. It is encouraging that filtering of these small features does not allow them to propagate into the interior or grow large in magnitude. If the horizontal grid resolution is sufficient to resolve the flow field, the removal of these spurious gravity waves should not affect the evolution of the fields of interest. It would be desirable to reproduce these calculations in a larger domain so that the boundary effects are further removed from the region of interest, but the high-resolution data is only available in the region of study.

6.1.2. Divergence equation

The horizontal divergence balance on day 28 is shown in Fig. 10. Throughout the duration of the simulation the dominant balance is between fR and D_2P. Only very small contributions are made by the linear balance and balance equation terms.

6.1.3. Kinetic energy equation

The kinetic energy balances at 1400 m are shown in Fig. 11. Prior to day 20 the kinetic energy is very small throughout the region. On day 20, Fig. 11a, the jet is beginning to develop along the eastern boundary At large scales, $\dot{K}$ (time rate of change) is balanced by ΔF_K (horizontal advection). At small scales, the horizontal and vertical pressure work balance in the northeast and southwest corners. This is a signal of the horizontal divergence seen in the vorticity equation terms. The horizontal pressure work (ΔF_π) is positive and the vertical pressure work (δf_π) is exporting energy vertically. The filter (F) is small in the region of the forming jet. Eight days later, Fig. 11b, the jet is becoming stronger with the maximum in K along the northern boundary. $\dot{K}$ is now balanced by ΔF_K and ΔF_π. There, δf_π is

still exporting energy in the vertical and b is just becoming noticeable in the northeast corner as available gravitational energy is being converted to kinetic energy. On day 36, Fig. 11c, the jet is beginning to weaken in the

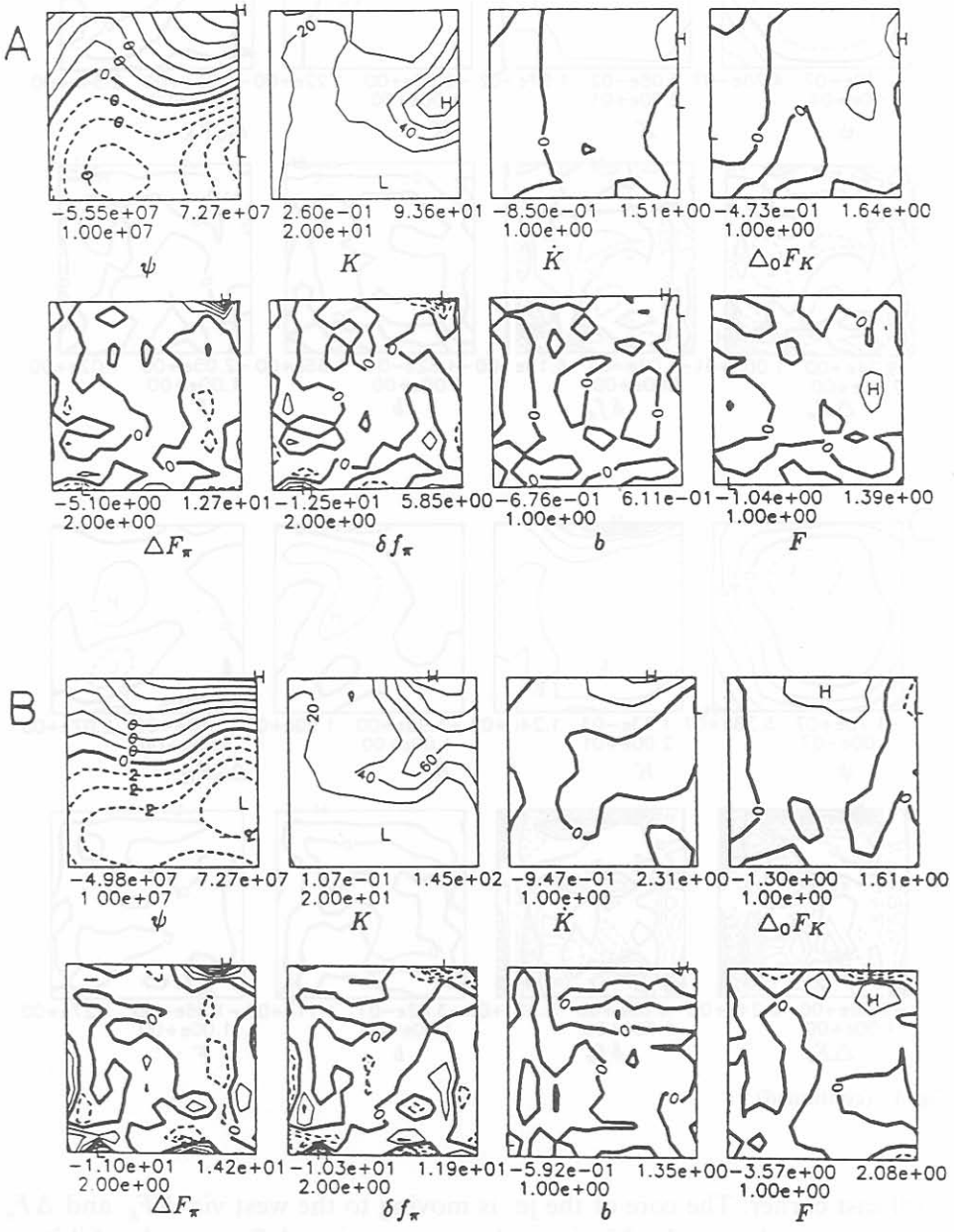

Fig. 11. PRE-EVA analysis: kinetic energy terms at 1400 m, (a) day 20, (b) day 28 (c) day 36 and (d) day 40.

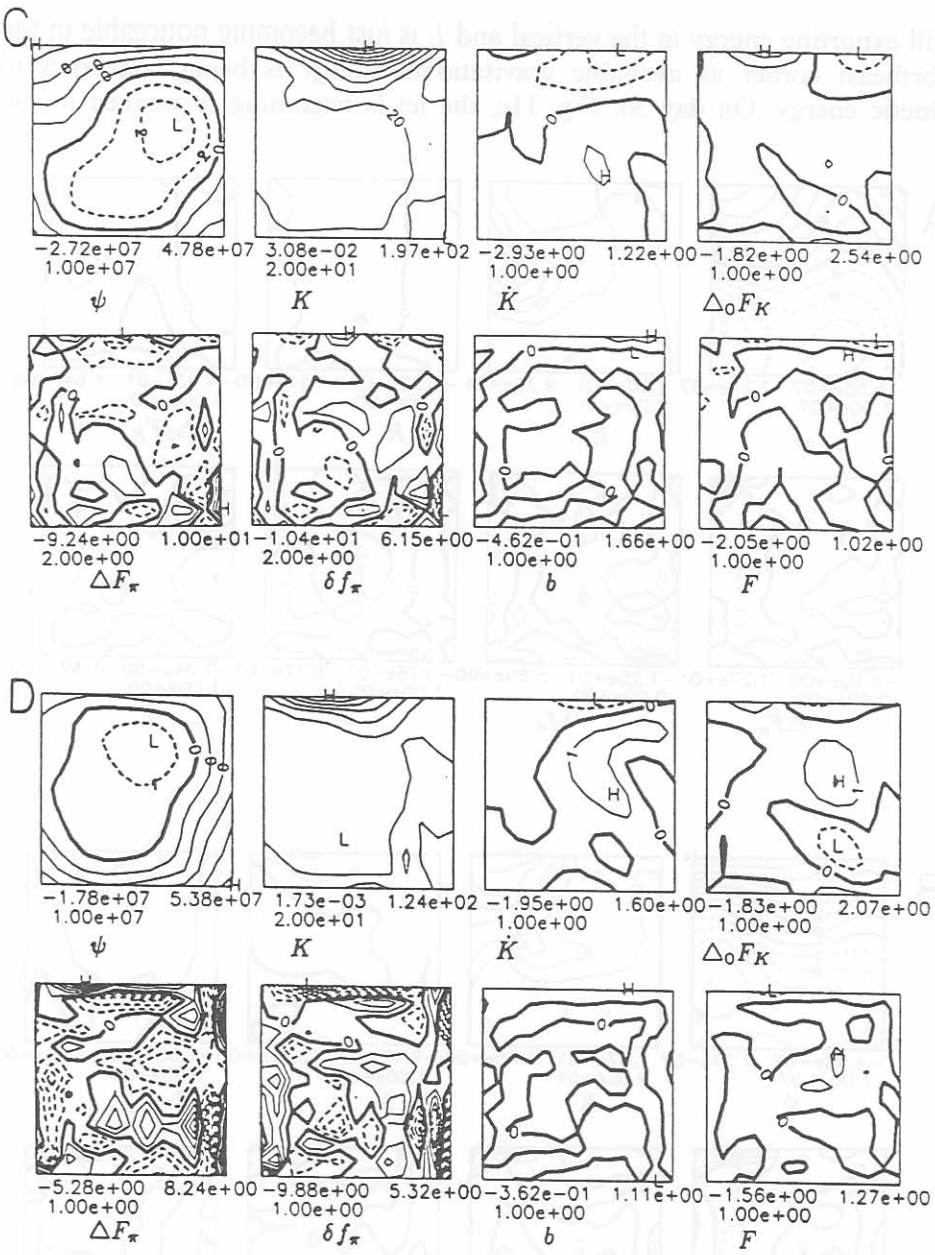

Fig. 11 (continued).

northeast corner. The core of the jet is moving to the west via ΔF_K and ΔF_π is moving to the north. δf_π is no longer negative definite and exhibits a small wavelike pattern. The baroclinic conversion is still present along the

northern edge of the region. Finally, on day 40, the jet has almost left the domain and $\dot{K}$, ΔF_K, b and F are small in that region, Fig. 11d. There is a strong balance between the pressure work terms, concentrated near and parallel to the boundaries. The development of the northeastward flow in the eastern half of the domain is evident in $\dot{K}$, ΔF_K, ΔF_π and δf_π.

6.1.4. Available gravitational energy equation

The available gravitational energy balances are shown in Fig. 12 at 1400 m. On day 20, Fig. 12a, the baroclinic structure of the jet is just becoming visible in the northeast corner of A. $\dot{A}$ (time rate of change) is balanced by ΔF_A (horizontal advection) and b (buoyancy conversion) is balanced by F (filter). This is very characteristic of the balances seen in the earlier equations. Eight days later, Fig. 12b, the dominant process is still ΔF_A, but there is also a net decrease of A in the jet region owing to the b–F balance. The jet has a strong baroclinic signature, but the rest of the region is relatively flat. A similar balance is seen on days 36 and 40, the dominant contribution to $\dot{A}$ is ΔF_A, with a net export of A owing to buoyancy conversion. This baroclinic conversion is consistent with the increasing barotropic structure of the jet. All of the important terms in the balance are included in quasi-geostrophic physics. The primitive equation vertical advection terms and horizontal advections by ageostrophic velocities are small throughout the analysis.

Away from the jet region, on days 36 and 40, b is converting A to K over most of the domain. This is coincident with the development of the strongly barotropic basin-scale cyclonic circulation seen in both the PE and QG model runs. This circulation is the major difference between the model calculations and the observed flow field. It is possible that the models have developed too strong a barotropic circulation because of the buoyancy conversion term. However, there may also be a problem with the barotropic component in the calculated observed flow fields. Several current meters, which are used to estimate the barotropic component, failed during the latter part of the integration period (Walstad, 1987).

To summarize, the signature of the jet formation and evolution is evident in each of the PRE-EVA equation balances. The relative vorticity terms exist on two separate scales. The evolution of large-scale vorticity along the meandering jet is dominated by horizontal advection processes, and the small-scale horizontal divergence is balanced by the filter. The divergence equation indicated that the geostrophic balance between the pressure and streamfunction terms is valid. The kinetic energy equation showed that the source of energy in the deep during jet growth was due to horizontal advection, horizontal pressure work and baroclinic conversion. Vertical pressure work exported some of this energy to the upper levels. The

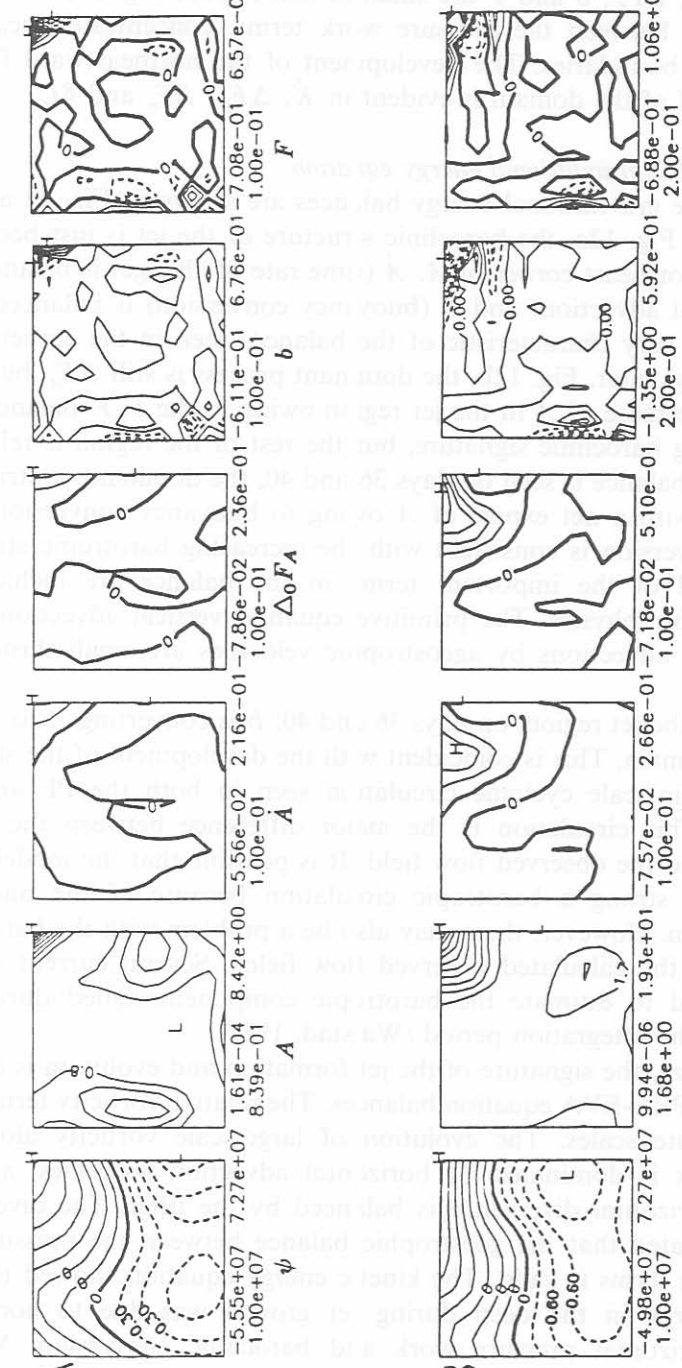

Fig. 12. PRE-EVA analysis: available gravitational energy terms at 1400 m, (a) day 20, (b) day 28, (c) day 36 and (d) day 40.

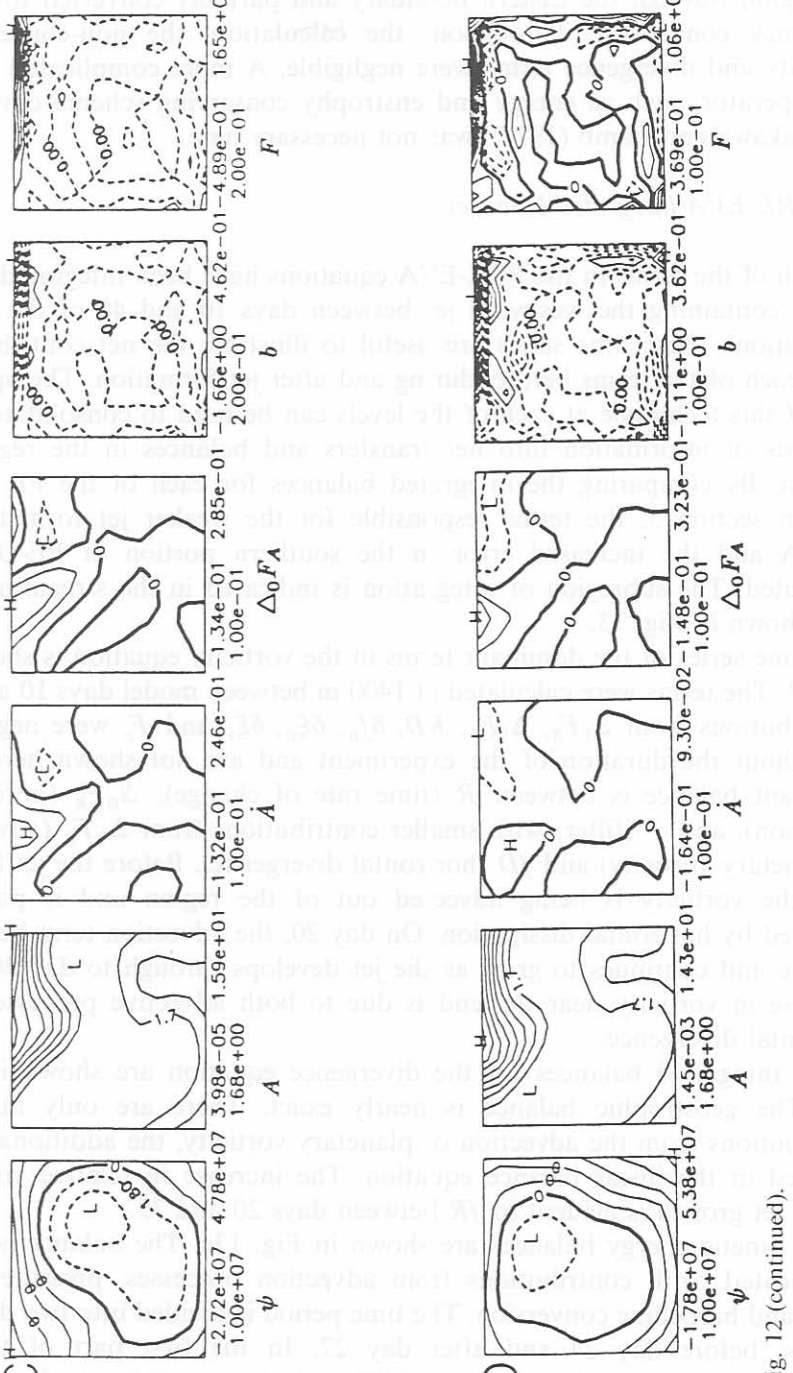

Fig. 12 (continued).

available gravitational energy balances indicated that A was advected into the region through the eastern boundary and partially converted to K via buoyancy conversion. Throughout the calculation, the non-conservative vorticity and divergence terms were negligible. A more complicated advection operator, such as energy and enstrophy conserving scheme developed by Arakawa and Lamb (1977), was not necessary here.

6.2. PRE-EVA integrated balances

Each of the terms in the PRE-EVA equations have been integrated in the region containing the westward jet between days 10 and 40 of the model integration. These time series are useful to illustrate the net contributions from each of the terms before, during and after jet formation. The application of this technique at each of the levels can be used to consolidate large amounts of information into net transfers and balances in the region of interest. By comparing the integrated balances for each of the PE model runs in section 5, the terms responsible for the weaker jet formation in PE-DA and the increased error in the southern portion of PE-OA are elucidated. The subregion of integration is indicated in the streamfunction map shown in Fig. 13.

A time series of the dominant terms in the vorticity equation is shown in Fig. 13. The terms were calculated at 1400 m between model days 10 and 40. Contributions from $\Delta_1 F_R$, $\Delta_1 F_P$, RD, δf_R, $\delta\xi_0$, $\delta\xi_1$ and F_z were negligible throughout the duration of the experiment and are not shown here. The dominant balance is between $\dot{R}$ (time rate of change), $\Delta_0 F_R$ (horizontal advection), and F (filter) with smaller contributions from $\Delta_0 F_P$ (advection of planetary vorticity) and fD (horizontal divergence). Before the jet formation, the vorticity is being advected out of the region and is partially balanced by horizontal dissipation. On day 20, the advection term becomes positive and continues to grow as the jet develops through to day 30. The decrease in vorticity near the end is due to both advective processes and horizontal divergence.

The integrated balances for the divergence equation are shown in Fig. 13b. The geostrophic balance is nearly exact. There are only minimal contributions from the advection of planetary vorticity, the additional term included in the linear balance equation. The increase in relative vorticity during jet growth is evident in fR between days 20 and 35.

The kinetic energy balances are shown in Fig. 13c. The balance is quite complicated, with contributions from advection processes, pressure work fluxes and baroclinic conversion. The time period is divided into two distinct periods, before day 27 and after day 27. In the first part of the jet development, the kinetic energy at 1400 m increases owing to horizontal

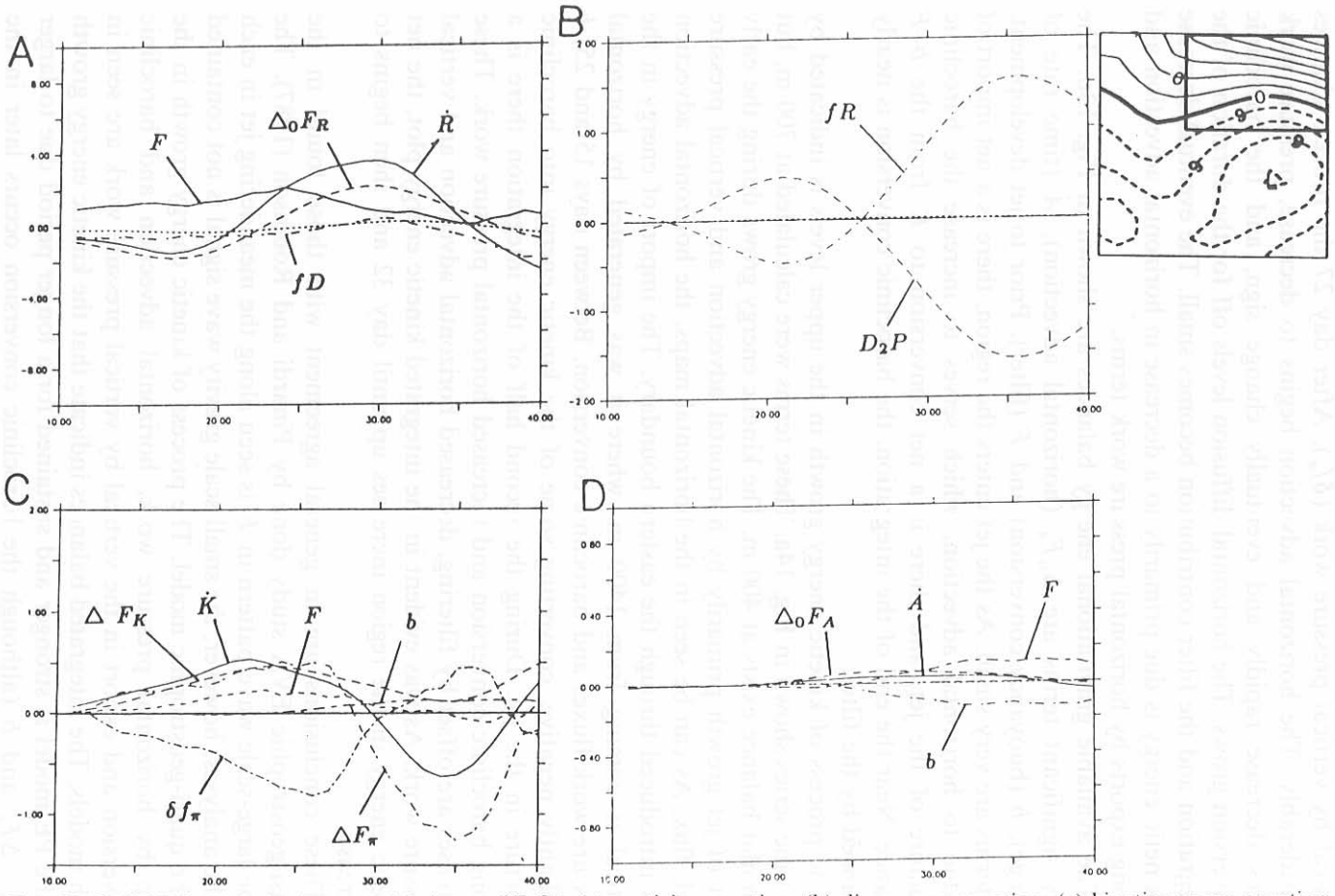

Fig. 13. PRE-EVA analysis: integrated balances PE-OA (a) vorticity equation, (b) divergence equation, (c) kinetic energy equation and (d) available gravitational energy equation.

advection (ΔF_K), horizontal pressure work (ΔF_π) and to a lesser extent filtering (F). These terms are balanced by a strong export of energy in the vertical by vertical pressure work (δf_π). After day 27 the process changes considerably. The horizontal advection begins to decrease, pressure work terms decrease rapidly and eventually change sign, and the baroclinic conversion grows. The horizontal diffusion levels off for the duration of the integration and the filter contribution becomes small. The eventual decrease in kinetic energy is due primarily to a decrease in horizontal advection and strong exports by horizontal pressure work terms.

The available gravitational energy balances are shown in Fig. 13d. The only significant terms are $\Delta_0 F_A$ (horizontal advection), $\dot{A}$ (time rate of change), b (buoyancy conversion) and F (filter). Prior to jet development, all terms are very small. As the jet enters the region, there is a net import of A due to horizontal advection, which serves to increase the baroclinic structure of the jet, and there is a net conversion to K from the b–F balance. Near the end of the integration, the baroclinic conversion is nearly balanced by the filter.

The process of kinetic energy growth in the upper levels is indicated by the time series shown in Fig. 14a. These terms were calculated at 700 m, but a similar balance exists at 400 m. The kinetic energy grows during the early part of jet growth primarily by horizontal advection and vertical pressure work flux. As can be seen in the horizontal maps, the horizontal advection was introduced through the eastern boundary. The import of energy in the vertical is coming from 1400 m, where it was generated by horizontal pressure work fluxes and baroclinic conversion. Between days 15 and 25, b is slightly negative, converting some of the kinetic energy into baroclinic structure in the jet. During the second half of the integration there is a strong baroclinic conversion and increased horizontal pressure work. These increases are offset by filtering, decreased horizontal advection and vertical pressure work. As was evident in the integrated kinetic energy plot, the net kinetic energy in the region increases up until day 32 and then begins to decrease.

These conclusions are in general agreement with those found in the quasi-geostrophic EVA study done by Pinardi and Robinson (1987). The same large-scale wave pattern in R is seen along the meandering jet in each of the analyses; however, the small-scale gravity wave signal is not contained in the quasi-geostrophic model. The process of kinetic energy growth in the deep by horizontal pressure work, horizontal advection and baroclinic conversion and export in the vertical by vertical pressure work are seen in both models. The integrated balances indicate that the kinetic energy growth in the PE model is stronger and sustained for a longer period due to larger ΔF_K, ΔF_π and b (although the baroclinic conversion occurs later in the

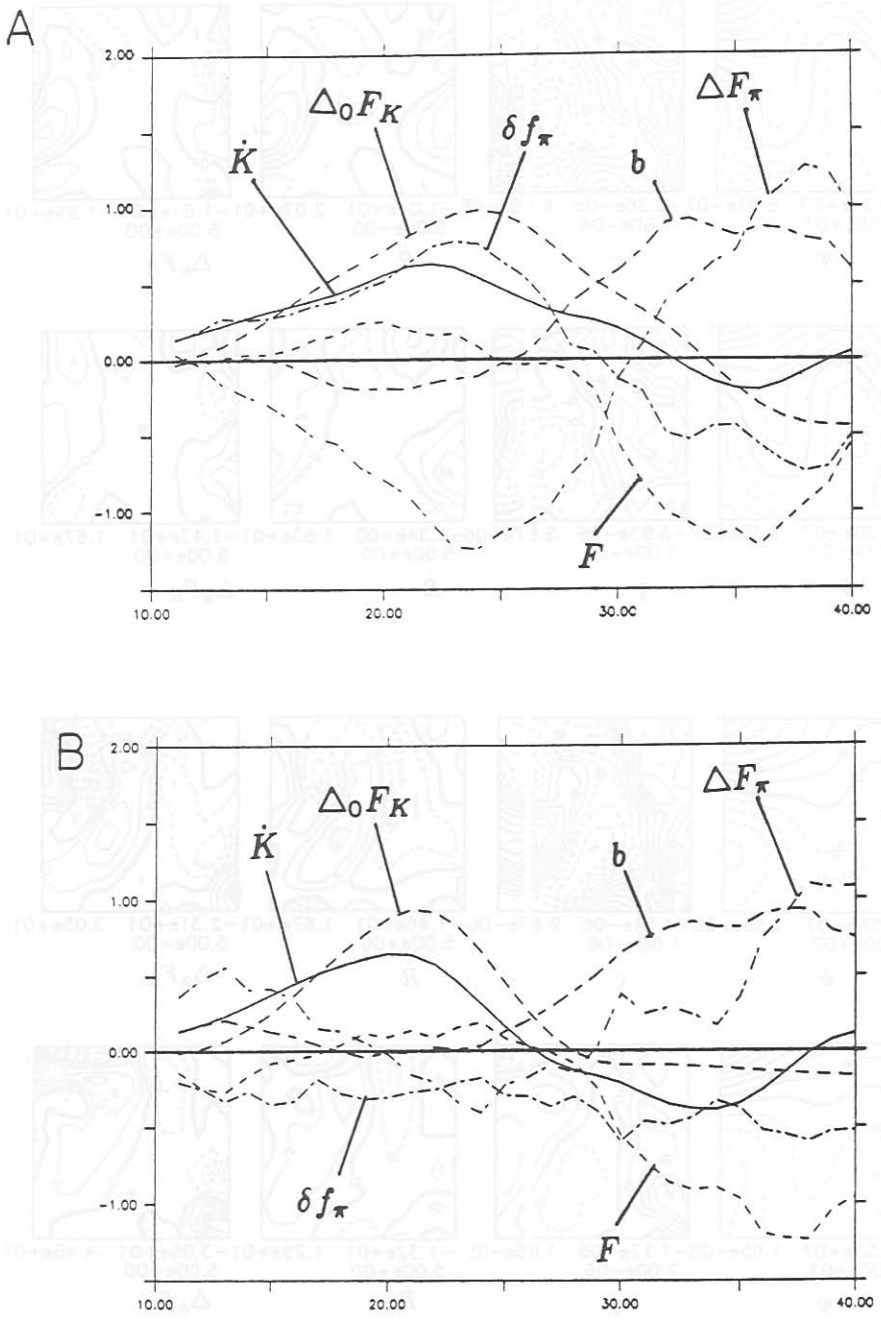

Fig. 14. PRE-EVA analysis: integrated balances kinetic energy equation (a) PE-OA and (b) PE-DA.

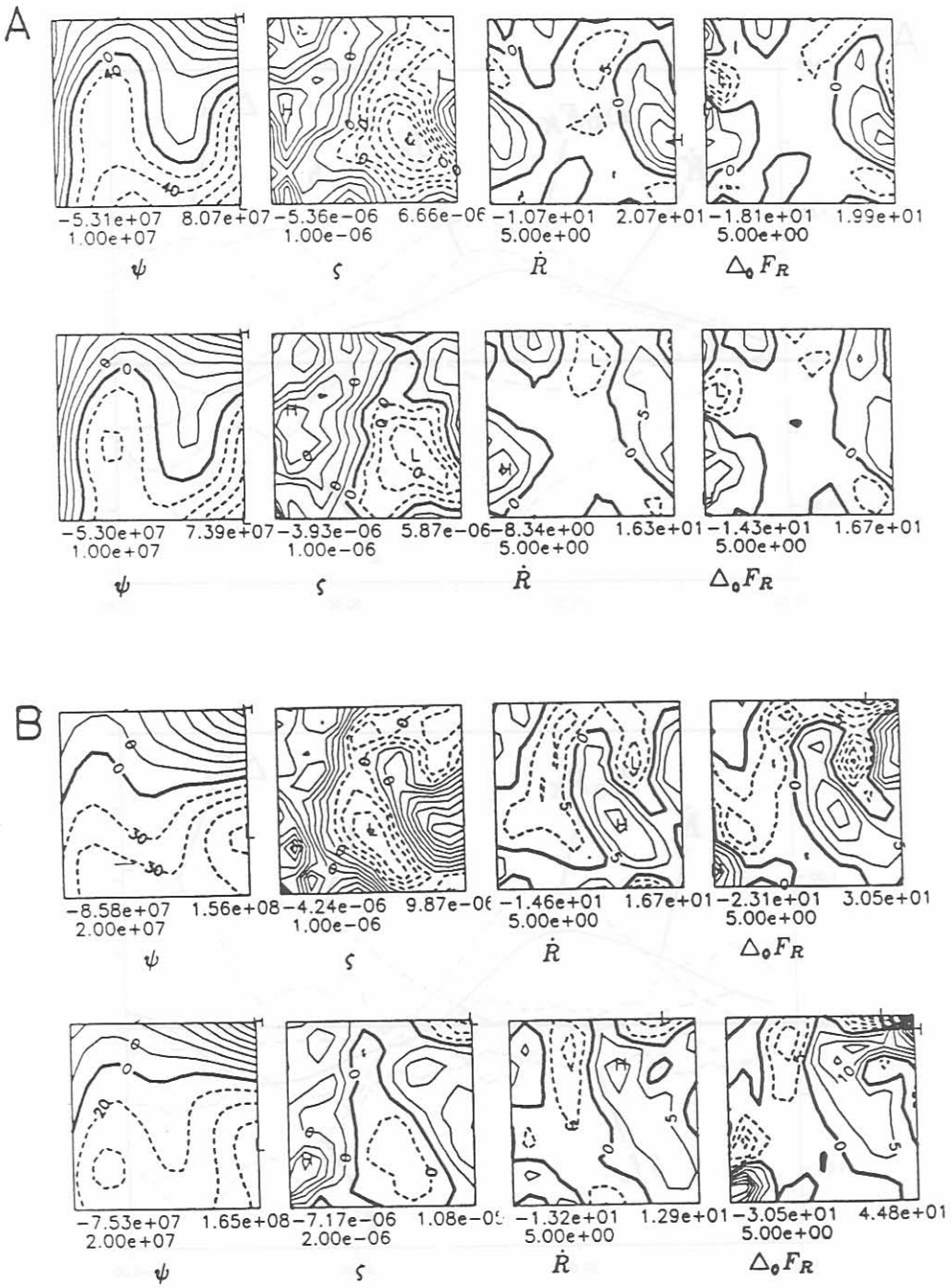

Fig. 15. PRE-EVA analysis: vorticity balances PE-OA (top row), PE-DA (bottom row), (a) day 12, (b) day 20 and (c) day 28.

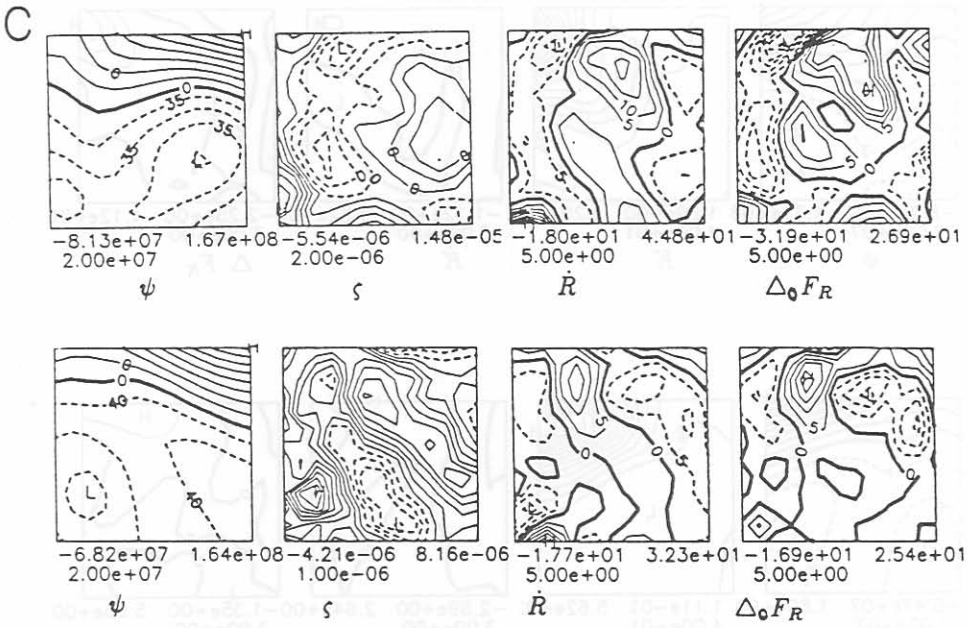

Fig. 15 (continued).

simulation). The vertical export of deep energy by δf_π is much stronger in the primitive equation fields. The available gravitational energy terms indicate a similar import of A by horizontal advection and conversion to kinetic energy in each model, however the filter is more active in the primitive equation calculations.

6.3. PRE-EVA analysis of PE-DA

In this section, the PRE-EVA analysis package will be applied to model simulations PE-DA and PE-OA in order to try to understand the differences in the model results. To summarize the findings of section 5, the development and maintenance of the westward flowing jet was reproduced better in PE-OA than in PE-DA.

Selected terms from the vorticity equation at 400 m are shown in Fig. 15(a–c). For each day, the top row is from calculation PE-OA and the bottom row is from calculation PE-DA. On day 12, Fig. 15a, the vorticity field looks almost the same for the two calculations. However, near the central part of the eastern boundary there is a patch of positive vorticity in PE-OA that is not as strong in PE-DA. The rate of change and horizontal advection terms indicate that this patch is being advected into the interior of PE-OA. On day 20, Fig. 15b, the large high in vorticity is seen extending

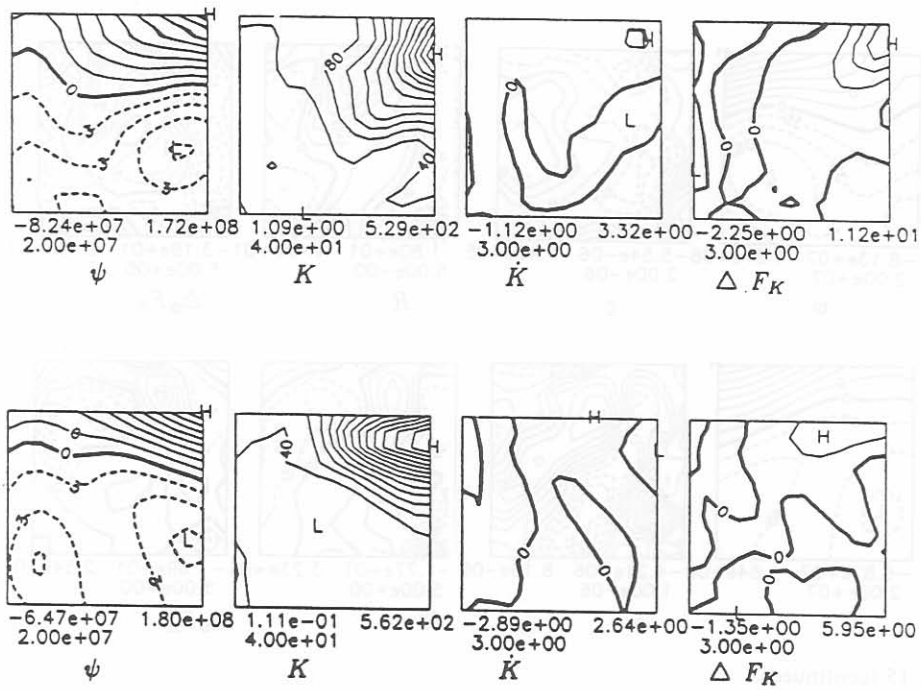

Fig. 16. PRE-EVA analysis: kinetic energy balances PE-OA (top row) and PE-DA (bottom row) day 24.

into the region through horizontal advections. The presence of this vorticity front is reflected in the southern central part of the streamfunction map. It is believed that this front is responsible for the increase in V_{NRMS} seen between days 15 and 30. On day 28, Fig. 15c, the jet is reaching its maximum strength. The vorticity front is near the western boundary, away from the region of jet formation.

The improved performance of PE-OA as compared with PE-DA in the jet formation region can be understood if we consider the kinetic energy balances. The basin-averaged kinetic energy plots shown in section 5.1 indicated that runs PE-DA and PE-OA were very similar until about day 22. Over the next 8 days the kinetic energy of PE-OA continued to increase, in good agreement with the observations, while that of PE-DA decreased. Selected terms from the kinetic energy equation at 400 m on day 24 for PE-OA and PE-DA are shown in Fig. 16(a and b), respectively. The magnitude of K is approximately the same but $\dot{K}$ is much different. The jet of PE-OA is still increasing in magnitude while the jet in PE-DA is decreasing. The primary contributor to this difference is ΔF_K. PE-OA is continuing to import K through the boundaries but PE-DA is not. This difference is also visible in the integrated balances at 700 m, Fig. 14a and b

for PE-OA and PE-DA, respectively. The horizontal advection terms have about the same magnitude at 22 days, but PE-DA decreases rapidly and PE-OA remains positive until day 34. There is a positive import of K via δf_π in PE-OA during jet development, which is not seen in PE-DA. This is the energy that was seen being exported via δf_π at 1400 m.

To summarize, use of boundary information that has been adjusted by the quasi-geostrophic model affected the PE model simulation in two ways. The cause of the local maximum in V_{NRMS} seen in PE-OA is due to a large vorticity front, which is advected into the region through the eastern boundary, ahead of the forming jet. The vorticity begins to enter the domain on day 12, is advected west, and on day 28 is just exiting out the western boundary. This vorticity was not advected into PE-DA because the QG model smoothed the data near the boundary. The improved jet formation in PE-OA is due to increased horizontal advection of K through the northeastern boundary and an import of energy due to vertical pressure work. This difference is also due to the inability of the QG calculation to sustain the small-scale wave pattern near the eastern boundary. This loss of resolution of the flow features in the QG model occurs within two grid points of the boundary and hence influenced the boundary conditions used in PE-DA. Additional resolution studies are needed to determine if this is a characteristic of the quasi-geostrophic equations or the numerical discretization used.

7. CONCLUSIONS

The open ocean hybrid coordinate PE model described by SR was applied to a hindcast study of the POLYMODE data set. Two 60-day simulations were carried out to determine: the feasibility of simulating real data with the regional PE model; the influence of using boundary conditions that have been dynamically adjusted with quasi-geostrophic physics; and the range of validity of quasi-geostrophy in the region.

The PE model correctly predicted the westward movement of a southward flowing jet, and the development and weakening of a strong westward jet. The fields compared well throughout the simulation; the NRMS difference in velocity between the primitive equation fields and the objectively analyzed data was less than 50% for the first 45 days. Basin-averaged vorticity and kinetic energy were reproduced well by the best PE simulation. These results indicate that the regional PE model can be used to simulate open ocean mesoscale eddy fields when sufficient data is available for initial and boundary conditions.

Comparisons were made between the primitive equation calculations and the best quasi-geostrophic calculation by W87. Although the NRMS velocity differences were generally slightly lower for the QG fields, the observed

basin-integrated kinetic energy and vorticity were reproduced better in the PE model. In addition, the density and velocity fields compared better with the data in the region of the westward jet for the best primitive equation calculation. When boundary conditions for the PE model were partially adjusted by the QG model the two calculations were very similar, both in terms of integrated quantities and direct comparisons. Although the jet formation was a little weak in the QG model, it is concluded here that quasi-geostrophic physics is relevant in the POLYMODE region.

A new primitive equation energy and vorticity analysis (PRE-EVA) routine was developed for use with the open ocean, hybrid coordinate PE model. The package solves the vertical vorticity, horizontal divergence, kinetic energy and available gravitational energy equations consistent with the PE model. PRE-EVA is applied diagnostically to fields generated by the numerical model. Analysis of term-by-term horizontal maps is used to elucidate the dominant processes of the flow. Each of the terms may also be integrated over critical subregions of the flow to highlight the net balances.

The PRE-EVA analysis package was applied to the best 60-day PE model calculation. The strong jet growth in the northern part of the domain was shown to be due to horizontal advection through the boundary, baroclinic conversion in the deep thermocline and vertical pressure work that exported the deep energy to the upper thermocline. Each of the important terms in the PRE-EVA equations were contained in quasi-geostrophic physics. The dynamical processes resulting from this analysis are in good agreement with the QG energetic analysis done by Pinardi and Robinson (1987), although the signal is somewhat stronger in the PE calculations. In the relative vorticity terms, there are two dominant balances, one small scale and one large scale. The small-scale balance is between horizontal divergence and filtering concentrated near the boundaries, believed to be caused by gravity waves. The large-scale balance contains the evolution of the mesoscale fields of interest. Efficient dissipation of the two-grid-point signal eliminates the gravity waves before they can propagate into the interior or interact at the scales of interest. These results indicate that the PRE-EVA analysis package can be used together with the regional PE model for the dynamic and energetic interpretation of observed mesoscale events.

Analysis of the primitive equation calculation that used the dynamically adjusted boundary conditions showed that the QG physics near the boundaries affected the primitive equation calculation in two ways. The advection of a vorticity front through the eastern boundary was significantly reduced and the strong jet growth in the northern part of the domain was weakened. Both of these differences are attributed to the inability of the QG calculation to sustain the small-scale wave pattern being advected through the eastern boundary. These results indicate that the PRE-EVA analysis

package is a useful tool for interpretation of differences between model calculations.

For the calculations presented here, the PE model was more expensive to run than the quasi-geostrophic model for two reasons. The CFL criterion for the maximum allowable time step is based on the fastest speed at which information can travel in the region (Courant et al., 1967). For the primitive equations, this is the internal gravity wave speed, $O(5\ \mathrm{m\ s^{-1}})$, but for the quasi-geostrophic equations it is generally the horizontal advection speed, $O(50\ \mathrm{cm\ s^{-1}})$ for POLYMODE. The time step used for the model calculations discussed here were 30 min and 360 min for the PE and QG models, respectively. In addition, the QG model is 2.5 times faster than the PE model per timestep, based on calculations in a $17 \times 17 \times 6$ model domain done on a SUN 110/FPA workstation. Based on these numbers, the PE model was 30 times more expensive to run than the QG model. For large numbers of calculations this may become an important consideration; however, both numerical models can play an important role in the simulation of mid-ocean mesoscale eddy regimes. The PE model was shown to be superior in the application discussed here, but the QG model captured the essential events at a fraction of the computational expense.

ACKNOWLEDGEMENTS

The author is grateful to Dr Leonard Walstad for discussions of the POLYMODE data set and making available his quasi-geostrophic calculations, and to Dr Nadia Pinardi for her review of the energy analysis section of this paper. This work was supported by the Office of Naval Research under contract number N00014-84-C-0461 to Harvard University.

APPENDIX

Aspects of the numerical solution procedure and a physical description of the PRE-EVA terms is given in this appendix.

The solution procedure for eqns. 4 and 5 separates the horizontal velocity field into an internal mode, $\bar{\mathbf{u}}$, and an external mode, $\hat{\mathbf{u}}$ as

$$\mathbf{u} = \bar{\mathbf{u}} + \hat{\mathbf{u}} \tag{A1}$$

where, for any variable μ

$$\bar{\mu} = H^{-1} \int_{-H}^{0} \mu \, \mathrm{d}z \tag{A2}$$

This leads to the definition of a transport streamfunction Ψ as

$$\bar{u} = -\frac{1}{H}\frac{\partial \Psi}{\partial y} \tag{A3}$$

$$\bar{v} = \frac{1}{H}\frac{\partial \Psi}{\partial x} \tag{A4}$$

This modal separation of the velocity vector is mentioned here because it will be important for the solution of the analysis equations.

Equations 15, 17, 19 and 21 are solved in the PRE-EVA package for analysis of fields generated by the open ocean PE model. Knowledge of the physical interpretation of each of these terms is essential in order to use the analysis package as a tool for diagnosis of the model results. A brief description of each of the terms in the above equations is as follows.

Vorticity equation terms

$\zeta : R$	relative vorticity
$\zeta_t : \dot{R}$	time change of relative vorticity
$J(\psi, \zeta) : \Delta_0 F_R$	advection of relative vorticity by geostrophic velocity
$J(\psi, f) : \Delta_0 F_P$	advection of planetary vorticity by geostrophic velocity
$f\nabla^2\chi : fD$	stretching of planetary vorticity
$\nabla\chi \cdot \nabla f : \Delta_1 F_P$	advection of planetary vorticity by irrotational velocity
$\nabla\chi \cdot \nabla\zeta : \Delta_1 F_R$	advection of relative vorticity by irrotational velocity
$\zeta\nabla^2\chi : RD$	stretching of relative vorticity
$w\zeta_z : \delta f_R$	vertical advection of relative vorticity
$\nabla w \cdot \nabla\psi_z : \delta\xi_0$	vorticity by twisting of geostrophic velocity fields
$J(w, \chi_z) : \delta\xi_1$	vorticity by twisting of irrotational velocity fields
$B\zeta_{zz} : F_z$	vertical diffusion
$F_h : F$	horizontal diffusion

Divergence equation terms

$\delta : D$	horizontal divergence
$\delta_t : \dot{D}$	time change of horizontal divergence
$\nabla^2(P/\rho_0) : D_2 P$	pressure term
$f\nabla^2\psi : fR$	coriolis term
$\nabla f \cdot \nabla\psi : \Delta_0 D_P$	geostrophic advection of the divergence supplied by the gradient of planetary vorticity
$J(f, \chi) : \Delta_1 D_P$	ageostrophic advection of the divergence supplied by the gradient of planetary vorticity

$\nabla \cdot [(k \times \nabla_\psi) \cdot \nabla (k \times \nabla \psi)] : \Delta_0 \Delta_0$	divergence of (geostrophic velocity advected by the geostrophic velocity)
$\nabla \cdot (k \times \nabla \psi) \cdot \nabla^2 \chi) : \Delta_0 \Delta_1$	divergence of (irrotational velocity advected by the geostrophic velocity)
$\nabla \cdot (\nabla \chi \cdot (k \times \nabla \psi)) : \Delta_1 \Delta_0$	divergence of (geostrophic velocity advected by the irrotational velocity)
$\nabla \cdot (\nabla \chi \cdot \nabla^2 \chi) : \Delta_1 \Delta_1$	divergence of (irrotational velocity advected by the irrotational velocity)
$\nabla w \cdot (k \times \nabla \psi)_z : \delta \Delta_0$	divergence by twisting of the geostrophic velocity fields
$\nabla w \cdot \nabla \chi_z : \delta \Delta_1$	divergence by twisting of the irrotational velocity fields
$BD_{zz} : F_z$	vertical diffusion
$F_h : F$	horizontal diffusion

Kinetic energy equation terms

$\frac{1}{2}(u^2 + v^2) : K$	kinetic energy
$\partial K / \partial t : \dot{K}$	time change of kinetic energy
$\nabla \cdot (\mathbf{u} K) : \Delta F_K,\ \delta f_k$	horizontal and vertical advection of kinetic energy
$\nabla \cdot (p / \rho_0 \mathbf{u}) : \Delta F_\pi,\ \delta f_\pi$	divergence of pressure work, horizontal and vertical
$g \Delta w : b$	buoyancy conversion
$BK_{zz} : F_z$	vertical diffusion
$F_h : F$	horizontal diffusion

Available gravitational equation terms

A	available gravitational energy
$\partial A / \partial t : \dot{A}$	time change of available gravitational energy
$\nabla \cdot (\mathbf{u}_0 A) : \Delta_0 F_A$	advection of A by geostrophic velocity
$\nabla \cdot (\mathbf{u}_1 A) : \Delta_1 F_A$	advection of A by ageostrophic velocities
$-(A/2s) w \partial s / \partial z : \delta \bar{\rho}$	source term due to mean stratification
$g \Delta w : b$	buoyancy conversion term
$BA_{zz} : F_z$	vertical diffusion
$F_h : F$	horizontal diffusion

PRE-EVA solution technique

The equations given in section 3 are in the continuous form as derived directly from the basic primitive equations. The PRE-EVA analysis actually

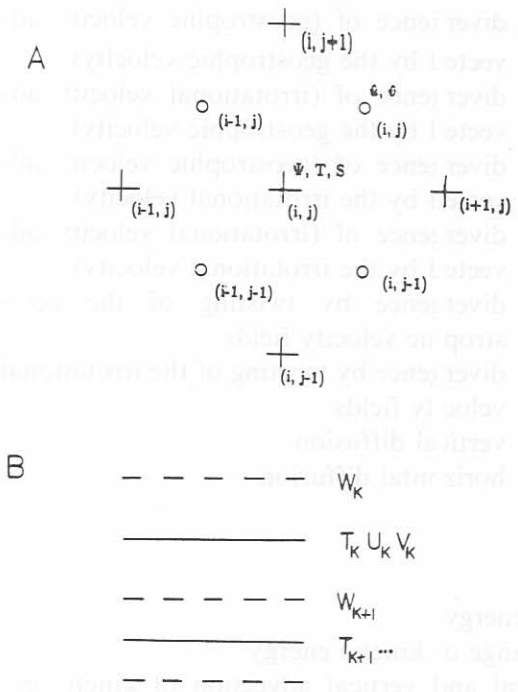

Fig. A1. B-grid distribution of grid points (a) horizontal and (b) vertical.

solves the finite difference representation of these continuous equations. Because the fields that are produced by the primitive equation model are valid for the particular grid representation and discrete advections used in the dynamical model, the finite difference version of the energy and vorticity analysis equations must be derived in such a way as to maintain this specific balance.

The differencing of the momentum equations used to derive the vorticity and divergence equations must be carried out so that the pressure terms cancel in the vorticity equation and add correctly in the divergence equation. This is accomplished by calculating each of the terms in the PRE-EVA equations at the T, S, Ψ points in the B-grid. Horizontal derivatives of the momentum equations use velocities at the four dots that surround the central plus in Fig. A1.

The advection terms in eqns. 4 and 5 must be separated into their advective and horizontal divergence components so that each of the terms in eqn. 15 can be represented. Because of the form of the Jacobian in the standard Bryan and Cox (1967) PE model does not conserve vorticity (M.D. Cox, personal communication, 1988), an extra term is introduced at this

step. It is an apparent source or sink of vorticity, which goes to zero as the grid spacing goes to zero; its form is given below

$$\left[\frac{(v_{i+1}+v_{i-1})(u_{i+\frac{1}{2}}-u_{i-\frac{1}{2}})}{2\Delta_x}+\frac{(v_{j+1}+v_{j-1})(v_{i+\frac{1}{2}}-v_{i-\frac{1}{2}})}{2\Delta_y}\right.$$
$$\left.+\frac{(v_{k+1}+v_{k-1})(w_{i+\frac{1}{2}}-w_{i-\frac{1}{2}})}{2\Delta_z}\right]_x-\left[\frac{(u_{i+1}+u_{i-1})(u_{i+\frac{1}{2}}-u_{i-\frac{1}{2}})}{2\Delta_x}\right.$$
$$\left.+\frac{(u_{j+1}+u_{j-1})(v_{i+\frac{1}{2}}-v_{i-\frac{1}{2}})}{2\Delta_y}+\frac{(u_{k+1}+u_{k-1})(w_{i+\frac{1}{2}}-w_{i-\frac{1}{2}})}{2\Delta_z}\right]_y$$

where the velocities at half-grid points are calculated from the internal and external modes at the interface between adjacent velocity points and Δ_x, Δ_y and Δ_z are the grid spacing in the x, y and z directions, respectively. $[]_x$ and $[]_y$ indicate derivatives in the x and y directions, respectively. Although generally small, this non-conservative term must be calculated and accounted for in the overall vorticity balance. The dependence of this term on the physical process being studied and the numerical discretization used may shed some light on the implications of a non-conservative advection scheme, such as that used in this PE model. Finite difference advective operators have been developed that conserve both energy and enstrophy (mean square vorticity) (Arakawa and Lamb, 1977), but they are considerably more complicated than that used here. For applications where the non-conservative term is large, these higher order advective operators may be desirable. A similar term arises in the horizontal divergence equation

$$\left[\frac{(v_{i+1}+v_{i-1})(u_{i+\frac{1}{2}}-u_{i-\frac{1}{2}})}{2\Delta_x}+\frac{(v_{j+1}+v_{j-1})(v_{i+\frac{1}{2}}-v_{i-\frac{1}{2}})}{2\Delta_y}\right.$$
$$\left.+\frac{(v_{k+1}+v_{k-1})(w_{i+\frac{1}{2}}-w_{i-\frac{1}{2}})}{2\Delta_z}\right]_y+\left[\frac{(u_{i+1}+u_{i-1})(u_{i+\frac{1}{2}}-u_{i-\frac{1}{2}})}{2\Delta_x}\right.$$
$$\left.+\frac{(u_{j+1}+u_{j-1})(v_{i+\frac{1}{2}}-v_{i-\frac{1}{2}})}{2\Delta_y}+\frac{(u_{k+1}+u_{k-1})(w_{i+\frac{1}{2}}-w_{i-\frac{1}{2}})}{2\Delta_z}\right]_x$$

Because the internal and external modes have been separated in the dynamical model solution, the individual components must also be treated separately in the calculation of the time rate of change in the vorticity and kinetic energy equations.

$$\frac{\partial\zeta}{\partial t}=\frac{\partial\bar{\zeta}}{\partial t}+\frac{\partial\hat{\zeta}}{\partial t}=(\bar{\zeta}^{\tau+1}+\hat{\zeta}^{\tau+1}-\bar{\zeta}^{\tau-1}-\hat{\zeta}^{\tau-1})/2\Delta_t \qquad \text{(A5)}$$

where

$$\bar{\zeta} = \left(\Psi_{i+1,j} + \Psi_{i-1,j} - 2\Psi_{i,j}\right)/H\Delta_x^2 + \left(\Psi_{i,j+1} + \Psi_{i,j-1} - 2\Psi_{i,j}\right)/H\Delta_y^2 \tag{A6}$$

$$\hat{\zeta} = \tfrac{1}{2}\left(\hat{v}_{i,j} + \hat{v}_{i,j-1} - \hat{v}_{i-1,j} - \hat{v}_{i-1,j-1}\right)/\Delta_x - \tfrac{1}{2}\left(\hat{u}_{i,j} + \hat{u}_{i-1,j} - \hat{u}_{i,j-1} - \hat{u}_{i-1,j-1}\right)/\Delta_y \tag{A7}$$

and

$$\frac{\partial K}{\partial t} = \frac{\partial \hat{K}}{\partial t} + \frac{\partial \overline{K}}{\partial t} = \left[\hat{u}\left(\hat{u}^{\tau+1} - \hat{u}^{\tau-1}\right) + \hat{v}\left(\hat{v}^{\tau+1} - \hat{v}^{\tau-1}\right) + \bar{u}\left(\bar{u}^{\tau+1} - \bar{u}^{\tau-1}\right) + \bar{v}\left(\bar{v}^{\tau+1} - \bar{v}^{\tau-1}\right)\right]/2\Delta_t \tag{A8}$$

The superscripts $\tau+1$ and $\tau-1$ refer to values at the next and previous time steps. In the absence of a superscript, the variable is assumed to be evaluated at the central time step. In practical applications, the next and previous times at which data has been saved from the dynamical model is generally more than one time step away from the central time. Some approximation is introduced into the time rate of change terms, but if the evolution of the fields is well resolved by the interval at which information is written to disk this error will be small. All other dynamical terms in the equations will be exact. The horizontal filter is calculated as a residual, and as a result, will reflect the error introduced by linearizing the time rate of change. The vertical diffusion terms are calculated at the central time step in the diagnostic package and, for reasons of computational stability, they are lagged by one time step in the dynamical model, this difference is negligible.

The equation used to derive the available gravitational energy equation was a single equation for density. In the dynamical model, the density is calculated by solving equations for temperature and salinity and using an equation of state to obtain density. In order to obtain an expression for the time rate of change of density which is consistent with the tracer equations solved in the numerical model, the following relation was used

$$\frac{\partial \rho}{\partial t} = \frac{\partial S}{\partial t}\frac{\partial \rho}{\partial S} + \frac{\partial T}{\partial t}\frac{\partial \rho}{\partial T} \tag{A9}$$

Where $\partial S/\partial t$ and $\partial T/\partial t$ are determined by the tracer equations in the numerical model and $\partial \rho/\partial S$ and $\partial \rho/\partial T$ are determined by the equation of state.

The buoyancy term (b) must be calculated so that it is equal and opposite in the kinetic energy and available gravitational energy equations. In deriving the kinetic energy equation, the hydrostatic equation is multiplied by w

and added to the horizontal components of the kinetic energy equation. In the numerical model, the momentum equations are calculated at levels and the hydrostatic equation is evaluated at interfaces. The proper weighting of the hydrostatic equation at the interface above and below the model level is used to obtain a consistent buoyancy conversion term.

REFERENCES

Arakawa, A. and Lamb, V.R., 1977. Computational design of the basic dynamical processes of the UCLA general circulation model. Methods Comput. Phys., 174–265.

Batteen, M.L., 1984. Numerical studies of mesoscale eddies using quasigeostrophic and primitive equation ocean models. Ph.D. thesis, Oregon State University, Corvallis, OR.

Bennett, A.F. and Kloeden, P.E., 1978. Boundary conditions for limited area forecasts. J. Atmos. Sci. 35: 990–996.

Bretherton, F.P. and Karweit, M.J., 1975. Mid-ocean mesoscale modelling. Numerical Models of Ocean Circulation. Ocean Affairs Board, Natural Research Council, NAS, Washington, DC, pp. 237–249.

Bryan, K. and Cox, M.D., 1967. A numerical investigation of the oceanic general circulation. Tellus, 54–80.

Bryden, H.L., 1982. Sources of eddy energy in the Gulf Stream recirculation region. J. Mar. Res., 40: 1047–1068.

Charney, J.G., Fjortoft, R. and von Neumann, J., 1950. Numerical integration of the barotropic vorticity equation. Tellus, 2: 237–254.

Courant, R., Friedrichs, K. and Lewy, H., 1967. On the partial differential equations of mathematical physics. IBM J., 215–234.

Daley, R., 1981. Normal mode initialization. Rev. Geophys. Space Phys., 19: 450–468.

Gent, P.R. and McWilliams, J.C., 1983. Regimes of validity for balanced models. Dyn. Atmos. Oceans, 7: 167–183.

Haidvogel, D.B., 1983. Periodic and regional models. In: A.R. Robinson (Editor), Eddies in Marine Science. Springer-Verlag, New York, pp. 404–437.

Haidvogel, D.B., Robinson, A.R. and Schulman, E.E., 1980. The accuracy, efficiency, and stability of three numerical models with application to open ocean problems. J. Comput. Phys., 34: 1–53.

Holland, W.R., 1978. The role of mesoscale eddies in the general circulation of the ocean—numerical experiments using a wind-driven quasigeostrophic model. J. Phys. Oceanogr., 8: 363–392.

Holland, W.R. and Lin, L.B., 1975. On the generation of mesoscale eddies and their contribution to the oceanic general circulation. i. A preliminary numerical experiment. J. Phys. Oceanogr., 5: 642–657.

Levitus, S. and Oort, A.H., 1977. Global analysis of oceanographic data. Bull. Am. Meteorol. Soc., 59: 1270–1284.

Lorenz, E.N., 1960. Energy and numerical weather prediction. J. Atmos. Sci., 19: 39–51.

McWilliams, J.C., 1983a. In: A.R. Robinson (Editor), Eddies in Marine Science. Springer-Verlag, New York.

McWilliams, J.C., 1983b. On the mean dynamical balances of the [gulf stream] recirculation zone. J. Mar. Res., 41: 427–460.

Miller, R.N., Robinson, A.R. and Haidvogel, D.B., 1981. A baroclinic open ocean model. J. Comput. Phys., 50: 38–70.

Oliger, O. and Sundstrom, A., 1978. Theoretical and practical aspects of some initial boundary value problems in fluid dynamics. SIAM (Soc. Ind. Appl. Math.) J. Appl. Math., 35: 419–446.

Orlanski, I., 1976. A simple boundary condition for unbounded hyperbolic flows. J. Comput. Phys., 21: 251–269.

Owens, W.B., Luyten, J.R. and Bryden, H.L., 1982. Moored velocity measurements on the edge of the [gulf stream] recirculation. J. Mar. Res., 40:509–524.

Phillips, N.A., 1966. The equations of motion for a shallow rotating atmosphere and the traditional approximation. J. Atmos. Sci., 626–628.

Phillips, N.A., 1969. The Dynamics of the Upper Ocean. Cambridge University Press, Cambridge.

Pinardi, N. and Robinson, A.R., 1986. Quasigeostrophic energetics of open ocean regions. Dyn. Atmos. Oceans, 10: 185–219.

Pinardi, N. and Robinson, A.R., 1987. Dynamics of deep thermocline jets in the POLYMODE region. J. Phys. Oceanogr., 17: 1163–1188.

Raymond, W.H. and Kuo, H.L., 1984. A radiation boundary condition for multidimensional flows. J. R. Meteorol. Soc., 110: 535–551.

Robinson, A.R., 1982. Dynamics of ocean currents and circulation: results of [polymode] and related investigations. A. Osborne and P.M. Rizzoli (Editors), Topics in Ocean Physics. Societa Italiana di Fisica, Bologna.

Robinson, A.R. and Walstad, L.J., 1987. The Harvard open ocean model: calibration and application to dynamical process, forecasting, and data assimilation studies. Appl. Numerical Math., 3(1–2): 89–131.

Robinson, A.R., Harrison, D.E., Mintz, Y. and Semtner, A.J., 1977. The general circulation of an idealized oceanic gyre: a wind and thermally driven primitive equation numerical experiment. J. Phys. Oceanogr., 7: 182–207.

Robinson, A.R., Carton, J.A., Pinardi, N. and Mooers, C.N.K., 1986. Dynamical forecasting and dynamical interpolation: an experiment in the California Current. J. Phys. Oceanogr., 13: 1561–1579.

Robinson, A.R., Spall, M.A. and Pinardi, N., 1988. Gulf Stream simulations and the dynamics of ring and meander processes. J. Phys. Oceanogr., in press.

Shapiro, R., 1970. Smoothing, filtering, and boundary effects. Rev. Geophys. Space Phys., 8: 359–387.

Shen, C.Y., McWilliams, J.C., Taft, B.A., Ebbesmeyer, C.C. and Lindstrom, E.J., 1986. The mesoscale spacial structure and evolution of dynamical and scalar properties observed in the [Northwestern Atlantic ocean] during the POLYMODE Local Dynamics Experiment. J. Phys. Oceanogr., 16: 454–482.

Spall, M.A., 1988. Regional ocean modelling: primitive equation and quasigeostrophic studies. Ph.D. Thesis, Harvard University, Cambridge, MA.

Spall, M.A. and Robinson, A.R., 1989. A new open ocean, hybrid coordinate primitive equation model. Math. Comput. Sim.

The MODE Group, 1978. The Mid-Ocean Dynamics Experiment. Deep Sea Res., 25: 859–910.

Walstad, L.J., 1987. Modelling and forecasting deep ocean and near surface mesoscale eddies: hindcasting and forecasting with, and coupling a surface boundary layer model to, the Harvard quasigeostrophic model. Ph.D. Thesis, Harvard University, Cambridge, MA 02138.